Chapter 31

Mouse Phenotyping with MRI

X. Josette Chen and Brian J. Nieman

Abstract

The field of mouse phenotyping with magnetic resonance imaging (MRI) is rapidly growing, motivated by the need for improved tools for characterizing and evaluating mouse models of human disease. Image results can provide important comparisons of human conditions with mouse disease models, evaluations of treatment, development or disease progression, as well as direction for histological or other investigations. Effective mouse MRI studies require attention to many aspects of experiment design. In this chapter, we provide details and discussion of important practical considerations: hardware requirements, mouse handling for in vivo imaging, specimen preparation for ex vivo imaging, sequence and contrast agent selection, study size, and quantitative image analysis. We focus particularly on anatomical phenotyping, an important and accessible application that has shown a high potential for impact in many mouse models at our imaging center.

Key words: MRI, magnetic resonance imaging, mouse, phenotyping, anesthesia, mouse handling, monitoring, central nervous system, cardiac, whole-body perfusion, excised organs.

1. Introduction

The mouse was the first live animal to be imaged using magnetic resonance imaging (MRI) (1), but following this initial demonstration, it was not utilized extensively. Historically, rats and guinea pigs were preferred for small animal imaging experiments due to their larger size, which allows for more satisfactory visualization of anatomy at limited image resolutions. However, the completion of the draft human and mouse genome sequences in the last few years has renewed interest in mouse MRI as a tool to investigate models of human disease, for which the mouse is the mammal of choice.

L. Schröder, C. Faber (eds.), *In Vivo NMR Imaging*, Methods in Molecular Biology 771,
DOI 10.1007/978-1-61779-219-9_31,

Toward the end of understanding the genome, there is now a worldwide effort to study genotype and phenotype—the physical and biochemical manifestation of a given genotype—with particular focus on relevant models of human disease. Both random and targeted mutagenesis methods have been explored and there is currently a consortium aiming to create mutants through conditionally knocking out each of the 23,000 genes in the mouse. While some diseases are associated with a specific gene (e.g., cystic fibrosis, Huntington's disease, and sickle-cell anemia), it is probable that many functional disorders result from a combination of subtle gene mutations. Thus, a vast number of mutant mice require characterization and phenotyping to identify the most useful disease models. This will be a time-consuming step, one in which MRI can play an essential role.

Disease model phenotypes can be characterized by studying anatomy, physiology, behavior, or function. Many of these tests can be performed in vivo, but the final step is to perform histopathology to look for organ, biochemical, and cellular differences. Given the enormous numbers of mouse mutants produced, it is difficult to characterize every mouse exhaustively and the potential for overlooking interesting phenotypes is high. By adapting the techniques and tools of MRI, which is inherently noninvasive, we are able to take detailed images of the inside of a mouse without conventional "slicing and dicing" and then perform phenotyping analyses computationally.

This form of mouse phenotyping with MRI is rapidly growing. Early approaches used conventional MRI techniques in conjunction with other phenotyping tests (2–4). In recent years, many more methodologies have been developed to enhance mouse phenotyping. The application most comparable to diagnostic radiology uses anatomical scans to look for size or morphology differences in organs, structures, or pathologies (5–8). Beyond anatomy, functional assays are possible by measuring blood–tissue perfusion (9, 10), ejection fraction in the heart (11, 12), and BOLD (blood oxygen level-dependent) response in the brain (13, 14). Other quantitative measurements related to tissue microstructure can be made by studying physical properties of water molecules in tissue, such as diffusion (15), relaxation parameters T_1, T_2 and T_2^*, or magnetization transfer (16, 17). Cerebral blood volume and fraction can also be measured quantitatively (18). Metabolism can be assessed with magnetic resonance spectroscopy (19), and, more recently, this has been done with hyperpolarized ^{13}C (20).

Anatomical scans, with contrast intended to highlight anatomical features, will remain an important component of mouse imaging studies as they are broadly applicable and are readily adapted to large-scale studies. Findings on anatomical images can then lead to further investigation by guiding histology. In brain studies, for instance, it has been shown that anatomical

MRI is very sensitive, with 87% of behavioral mutants also showing a neuroanatomical phenotype (21). This represents a remarkable link between anatomy and function and suggests anatomical phenotyping is a powerful investigative tool. Even when qualitative radiological inspection cannot detect phenotypic differences, detailed computational analysis can reveal subtle differences by group comparisons (22).

The most vital part of image-based phenotyping starts with high-quality image data. Often, this will require images in several control and mutant animals, or in several animals at multiple time points. The group sizes required will depend on the subtlety of the phenotype in question, with larger groups required as phenotypes become more nuanced. As the number of mice studied increases, imaging throughput becomes essential and implementation of multiple-mouse MRI (23), in which several mice are imaged simultaneously in the same MRI scanner, is extremely beneficial. In this chapter, we will describe general methods to acquire quality images for mouse phenotyping and discuss subsequent analysis methods. We emphasize techniques that best allow for quantitative anatomical phenotyping in which differences between mice can be demonstrated and measured, but also mention other imaging methods providing alternative phenotyping possibilities.

2. Materials

2.1. MRI System

The most obvious difference between imaging mouse versus man is the size of the subject; the requisite increase in resolution for mouse images results in fewer protons per image voxel and lower signal-to-noise ratios in the mouse. To account for this, higher field magnets are preferred as they increase signal strength.

1. It is possible to begin mouse imaging using available clinical scanners and associated hardware and software (24). However, a dedicated *small-animal, high-field magnet* (>7 T) is much preferred. The two major vendors for small animal imaging are Bruker Biospin MRI GmbH (Ettlingen, Germany) and Agilent Technologies, Inc. (formerly Varian, Inc., Palo Alto, CA). The descriptions below about animal handling and imaging applications are largely independent of the magnet choice.
2. If only a clinical scanner is available, hardware limitations can be largely eliminated by using a *purpose-built insert gradient coil* with high slew rates and gradient strengths (25). In combination with the animal-specific hardware listed below, this will achieve significantly improved image resolution and

quality and may represent a good alternative to a dedicated animal system.

3. According to the organ or system being studied, an *application-specific radiofrequency coil* should be chosen. For example, in the case of the eye, a small surface coil is needed. If, on the contrary, the whole mouse is of interest then a birdcage volume coil encompassing the entire mouse is required. Small animal MRI system manufacturers, including Bruker and Varian, offer coils and major independent sellers include Doty Scientific, Inc. (Columbia, SC) and RAPID Biomedical GmbH (Rimpar, Germany). Multiple coil arrays for spatially-sensitive encoding, analogous to standard practice on human clinical systems, are likely to become more commonplace in animal systems as well.
4. The Mouse Imaging Centre has implemented a multiple-mouse MRI system on the Varian architecture, which is designed to allow their hardware to be scalable. The key benefit to such a system is the capability for more imaging-intensive, high-throughput studies. Along with a wide-bore, horizontal magnet, *multiple transmit/receive channels and multiple coils* are required (each channel accommodates one mouse).

2.2. Mouse Handling

1. All mouse research requires local ACC (Animal Care Committee), IACUC (Institutional Animal Care and Use Committee) or equivalent approval for mouse-handling procedures.
2. An *anesthetic* is needed to sedate the mouse during in vivo imaging experiments; gaseous isoflurane or injectable ketamine/xylazine mixtures are most common. For functional MRI studies, some investigators prefer α-chloralose as an alternative because it does not depress cardiovascular response as significantly as other agents.
3. If an inhalation anesthetic is used, then *oxygen* and associated *tubing* is necessary to deliver the anesthetic to the animal. A *scavenger* system is also required to properly and safely eliminate the anesthetic from the MRI room (there are passive and active models at Paragon Medical, Coral Springs, FL).
4. Mice under sedation cannot maintain their own body temperature, especially in air-conditioned magnet rooms; therefore a *heat source* (e.g., forced air or recirculating water bath), needs to be used. We specifically use model F7001 from Edemco Dryers, Colorado Springs, CO for multiple mice. A less powerful version is needed for single mice. In conjunction, a *proportional–integral–derivative*

controller (PID controller) is needed to create a feedback loop to maintain a constant temperature for the mouse (e.g., Omron Electronics, worldwide offices).

5. A *temperature probe* is used to monitor the temperature of the mouse. The internal temperature can be monitored with a rectal probe or the skin temperature can be monitored with a probe on the skin (we use a t-type thermocouple positioned at the abdomen from Omega Engineering Inc., Laval, Canada).
6. The monitoring of heart rate requires *ECG connectors* (pads, copper tape, or needle varieties are widely available. We use non-magnetic neonatal/pediatric ECG electrodes from ConMed Corp., Utica, NY). If using tape or pads, hair from the contact points (chest or limbs) must be removed with a *razor or depilatory cream*. Applying *ECG gel* helps improve electrical contact. Since the monitoring of the mouse will be taking place inside a magnetic field, non-magnetic electrical connections are preferred. Furthermore, to prevent interference from the gradients with physiological signals, either fiber-optic connections (26) or analog filters are beneficial.
7. The monitoring of the breathing rate requires *respiratory pillows or bellows* (we use pillows from Smiths Medical, various worldwide distribution sites).
8. While most of the monitoring equipment can be developed in house with basic electronics, *animal monitoring systems* can be purchased as a single unit from commercial vendors, such as the system made by SA Instruments, Inc. (Stony Brook, NY), Biopac Systems, Inc. (Goleta, CA) or Rapid Biomedical (Rimpar, Germany). These devices can also be interfaced with the MRI system for triggering or gating.
9. An *animal cradle* helps with reproducible mouse positioning and can have integrated physiological monitoring components. Sometimes *motion restraints* (e.g., Velcro or tape) are helpful to prevent motion artifacts (*see* **Fig. 1**). These can be developed in-house or are available from Dazai Research Instruments, Toronto, Canada.
10. Other miscellaneous items include *saline* and *syringes* as well as *gloves* and *laboratory coats or surgical gowns* for mouse handling.

2.3. Contrast Agents

The use of contrast agents is often beneficial to highlight particular anatomical features or to permit more rapid imaging.

1. The most common contrast agent is *gadolinium* (Gd), administered in a chelated form that keeps it in the extracellular space or bloodstream. Sometimes it is injected into

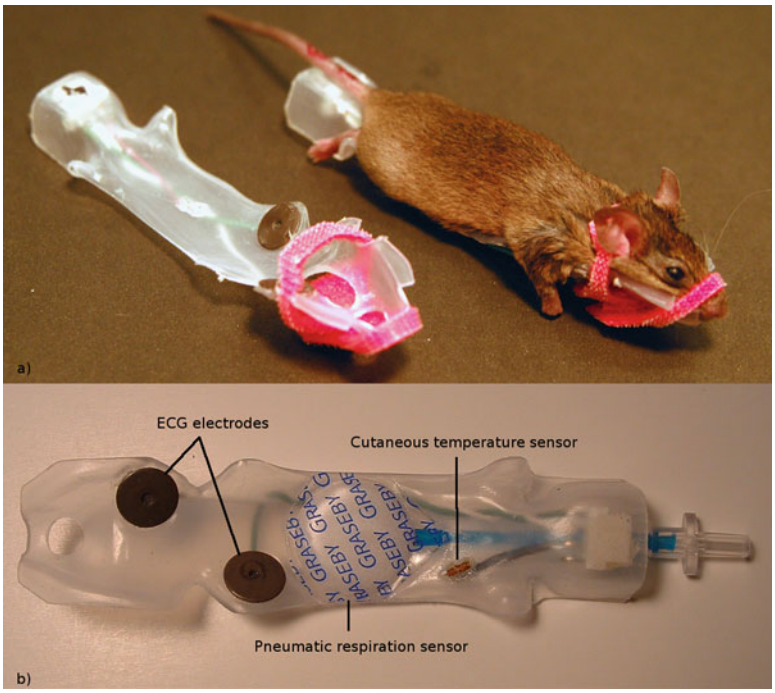

Fig. 1. The mouse sled used to position the mouse and provide physiological contacts (36). (**a**) The sled indicating the Velcro attachment to secure the mouse's head. (**b**) A close-up of the mouse sled with sensors labeled. Pictures provided courtesy of Jun Dazai.

the mouse before a scan to decrease T_1 relaxation times and permit faster imaging (e.g., 0.1 mM/kg gadopentetate dimeglumine (Berlex, Lachine, Quebec, Canada)) or to highlight pathology that breaks down the blood–brain barrier. If studying the vasculature or blood flow, various methods of time-of-flight angiography or perfusion measurements can be performed by saturating or inverting the signal in a volume of interest and then imaging signal effects during blood inflow (27, 28).

2. *Manganese* (Mn) is a useful contrast agent in the mouse that is not available to use in humans. It is most commonly used for imaging of the central nervous system, acting as a calcium analogue that is taken up across cellular calcium channels. The uptake of Mn by different parts of the brain depends on time and careful attention to the timing of injection can highlight specific parts of the brain (29). To generally decrease the T_1 time, we have injected 20 mg/kg $MnCl_2$ intraperitoneally 48 h prior to imaging (30).
3. In contrast to Gd and Mn agents, *iron oxide particles* create "negative contrast," a dark region in the MR image. These agents can be administered for functional vasculature measurements particularly in connection with solid tumors

(e.g., 0.5 mol Fe/L Resovist, Schering, Berlin, Germany). Additionally, they continue to be experimented with for cellular imaging applications, in which a cell population of interest is labeled either in vitro or in situ and then tracked for migration in normal or disease conditions (31–33).

2.4. Postmortem Imaging of Excised Organs

MRI can approach microscopic resolutions when motion is eliminated and scan time is not a limiting factor. Postmortem imaging of fixed tissue specimens therefore results in images that provide more detailed anatomy than can be achieved in vivo. Typically, an open-heart perfusion (*see* **Section 3.3.4**) is performed to fix the organs—and optionally to perfuse the mouse with contrast agent—and then the organs of interest are excised.

1. Injection anesthetic (e.g., Avertin, Sigma-Aldrich, worldwide offices)
2. Syringe and needle
3. Scalpel
4. Heparin (10 units/mL)
5. Saline
6. Contrast agent (optional, e.g., 2 mM ProHance, Bracco Diagnostics, Inc., worldwide offices)
7. Fixative (formalin)
8. Proton-free susceptibility matching fluid (e.g., Fluorinert, 3 M, Maplewood, MN)
9. NMR sample tube
10. Ultrasound biomicroscope (Vevo 770, VisualSonics, Toronto, Canada)
11. Gloves and goggles

2.5. Computation

After acquiring image data, a computing platform is required to visualize and analyze the data. The type of image analysis will depend heavily on the phenotypes of interest. We focus here on common needs for anatomical phenotyping.

1. A *workstation* with satisfactory memory, disk space, and speed is critical. It is most important to have ample RAM (random access memory) especially if the datasets are large. We typically work with images that are 0.5 GB in size, which require about 2–4 GB of RAM. It is also beneficial to have the fastest processors available (minimum 2 GHz) with ample diskspace. Having a good video card with minimum 512 MB facilitates smooth visualization of large 3D datasets. We have found a Linux-based workstation to be generally most cost effective, but it requires more computer savvy. Most commercial software licenses are available in both PC and Macintosh flavors.

2. To look at the data, *visualization software* is needed. There is freeware available on the internet, such as ImageJ (National Institutes of Health, http://rsbweb.nih.gov/ij/), OCCIviewer (University of Toronto, http://www.cardiacimaging.ca/technical_resources/occi_viewer/), and Display (McGill University, http://www.bic.mni.mcgill.ca/software/), though for more complicated 3D renderings, commercial software (e.g., Amira, http://www.amiravis.com/ or Analyze, http://www.analyzedirect.com/) is often better suited.
3. *Registration and segmentation software* are used to align and identify anatomical structures in images. Results from these image-processing steps are crucial for finding subtle phenotypes by computational methods. Popular open source software include SPM (Statistical Parametric Mapping, University College London), ITK (Insight Segmentation and Registration Toolkit), Automated Image Registration (University of California, Los Angeles), and Image Registration Toolkit (Imperial College, London); commercial versions are available as well (e.g., 3D-DOCTOR, Able Software Co., Lexington, MA and BrainVoyager, Maastricht, the Netherlands).
4. To conduct *statistical analysis*, software such as R and MATLAB (Mathworks, Natick, MA) are very powerful. There are a few pre-assembled MATLAB packages such as SurfStat (http://www.math.mcgill.ca/keith/surfstat/) and Partial Least Squares (http://www.rotman-baycrest.on.ca/index.php?section=84). Other packages are NIPY (Neuroimaging in Python, http://neuroimaging.scipy.org/site/index.html) and RMINC written in R (https://launchpad.net/rminc). We have found Python (http://www.python.org) and Perl (http://www.perl.org) to be good programming environments for establishing analysis pipelines for large multi-image datasets.

3. Methods

3.1. Animal Preparation for In Vivo Imaging

One of the advantages of MRI is the ability to image the mouse in vivo, which allows for longitudinal studies in individual subjects. In many experiments, this is preferred over imaging or histology of many different mice at set time points because it allows progress of disease—such as a spontaneous tumor—in the same animal to be followed over time (*see* **Note 1**). The overall goal in preparing an animal for live imaging is to place an anesthetized

mouse in a consistent position (*see* **Note 2**) with various physiological monitoring devices attached. Rapid preparation time is required to accommodate several imaging sessions per day and dependable positioning facilitates image comparison after image acquisition.

1. To perform in vivo imaging requires maintaining and monitoring the physiology of the mouse during imaging sessions. A recent review discusses usage of different anesthetics for MR (34). In general, inhalation anesthetics, such as isoflurane and halothane, are employed as they are easy to control and are fairly gentle to the animal (*see* **Note 3**). Induction of the mouse is typically achieved with 3–4% isoflurane and then maintained at 1% isoflurane in 100% oxygen.
2. After induction, mice should be intraperitoneally injected with saline prior to imaging to prevent dehydration during long scanning sessions (roughly 0.2–0.4 mL/30 g/h).
3. Once under anesthesia, the mouse should be monitored via the temperature probe, ECG, and respiratory pillow. Supplemental monitors of physiological state may include exhaled CO_2, blood pressure, or blood oxygenation, although these are not routinely necessary for anatomical imaging.
4. In our experience, using forced air heating, we have found that C57/Bl6 mice are best maintained when the magnet bore temperature is at 27°C, which results in a skin temperature of 30°C (*see* **Note 4**). Maintaining good temperature control is not only important for the mouse, but in fact results in improved image quality (35). The type of heat source selected may be application dependent (*see* **Note 5**).
5. Beyond simple monitoring of the mouse, some experiments require gating on either or both the cardiac and the respiratory signals. The signal from the ECG and respiratory monitoring system are used for this purpose (*see* **Note 6**).

3.2. Considerations for Multiple Mice

Delays associated with animal handling are exacerbated when dealing with multiple mice simultaneously for a multiple-mouse MRI experiment. Since it is important to minimize the time each mouse is under anesthesia, every attempt should be made to streamline the process of preparing individual mice. This is so that the total duration of anesthesia for the mice is not unnecessarily extended because multiple mice are being prepared. In our laboratory, we have devised several shortcuts to reduce the preparation time for seven mice to less than half an hour (36). We direct interested readers to this reference for further details.

3.3. Data Acquisition

A powerful aspect of MRI is the flexibility to study various phenotypes in the mouse. Different organ systems can be studied with careful positioning of either a surface coil or a small volume

coil. Once focused on the region of interest, both anatomy and function can be studied by choice of pulse sequence. A complete review of available pulse sequences is beyond the scope of this chapter. In general, MR sequences in routine use clinically provide visualization of anatomy, morphology, or pathology. Perfusion, diffusion, flow, and other functional measures require more sophisticated imaging sequences, although many of these are used routinely in research studies in both humans and mice (*see* **Note 7**). These are discussed in more detail in other chapters. In the next sections, we will discuss several imaging considerations and procedures for mouse phenotyping.

3.3.1. Anatomy

1. It is important in anatomical phenotyping to ensure good contrast between relevant structures. At higher field strengths, longitudinal relaxation times (T_1) increase and become less distinct, so for the most part, T_2-weighted images are preferred amongst the intrinsic image contrasts available. **Figure 2** shows several examples of T_2-weighted images.
2. Administration of Mn intraperitoneally 24 h prior to imaging of the brain is a popular way of obtaining neuroanatomical contrast in the mouse brain. Differential uptake of the Mn highlights different structures in T_1-weighted images because Mn is paramagnetic and locally shortens the T_1 relaxation time. Interestingly, Mn is transported along axons and can traverse synapses and has also been used for tract tracing after focal injections. **Figure 3** shows an example of a manganese-enhanced brain.
3. Another alternative for contrast within the central nervous system is to use diffusion-weighted imaging (15), which can differentiate diffusion rates of water parallel or perpendicular to the axis of a neuron. Recently, in vivo techniques have advanced so much so that fiber tractography, which follows fiber connectivity, can be performed in live mice (**Fig. 4a**) (37).
4. Another application of diffusion tensor imaging is to calculate the fractional anisotropy, which is the scalar value between 0 and 1 that describes the degree of anisotropy of white matter fibers. A value of 0 means that diffusion is isotropic and a value of 1 means that diffusion occurs only along one axis and is fully restricted along all other directions (**Fig. 4b**). Many other diffusion variants are also possible (38, 39).

   Although the majority of mouse studies to date have focused on the brain or the heart, most of the organs within the mouse have been imaged and phenotyped. A notable phenotyping endeavor is diabetes and obesity. In this

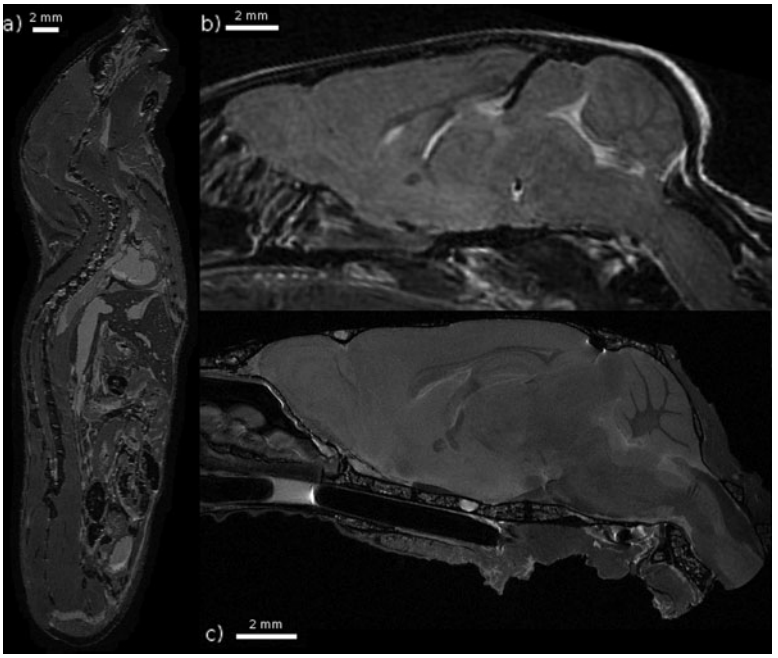

Fig. 2. Three examples of T_2-weighted mouse images taken at 7 T. (**a**) A fixed whole mouse prepared by perfusion fixation with ultrasound guidance (Ref. (101)) including 10 mM Magnevist. A spin echo sequence was used with TR/TE = 650/15 ms and $(100\ \mu m)^3$ voxels resulting in an imaging time of 13 h. (**b**) A brain imaged in vivo. A fast spin echo sequence was used with cylindrical acquisition, TR/TE = 900/12 ms, with TE_{eff} = 36 ms, echo train length 8, two averages, flip angle 40°, matrix size 400 × 240 × 240, resolution $(100\ \mu m)^3$ resulting in an imaging time of 2 h and 50 min (Ref. (119)). (**c**) A fixed brain prepared by perfusion fixation with 0.5 mM ProHance (Bracco Diagnostics, Inc.). After fixation, the skull is separated from the body. A fast spin echo sequence was used with TR/TE = 325/6 ms, with TE_{eff} = 30 ms, echo train length 6, four averages, matrix size 780 × 432 × 432, resolution $(32\ \mu m)^3$ resulting in an imaging time of 11.3 h. Figure provided courtesy of Christine Laliberté.

instance, anatomical images of the whole body need to be acquired.

5. In these applications, fat and water images can be separated based on their relative chemical shift via various methods (i.e., the Dixon technique). Volumetric measurements further permit the amount of fat to be quantified (40). Other sites of investigation have included the optic nerve (41), spinal cord (16, 42), liver (43, 44), kidneys (45), prostate (46), and pancreas (47). Initial selection of particular sequences for visualization in any of these organs or structures can be guided by existing literature studies.

3.3.2. Imaging in the Chest and Abdomen

1. In general, anatomy of interest distant from sites of physiological motion can be secured to prevent motion artifacts in images. For instance, we use specially cut Velcro to secure

Fig. 3. A coronal (*top*) and sagittal (*bottom*) view of an in vivo mouse brain imaged with $MnCl_2$ injected as a contrast agent. The $MnCl_2$ was intraperitoneally injected 24 h prior to imaging. The T_1-weighted spin echo sequence had the following scan parameters: TR/TE = 90/3.8 ms, flip angle 55°, resolution = (115 μm)^3 and scan time = 2 h. With no manganese, the contrast is very flat but in the image it can be seen that the Mn^{2+} is taken up by the layers of the cerebellar folia (cerebellum, cb), the hippocampus (hc), the olfactory bulbs (ob) as well as in the pituitary gland (pg).

the head during brain imaging (*see* **Fig. 1**). Another simple method to minimize motion artifacts is to place the mouse in a supine position, such as for imaging of the kidneys (45) or spine.

Fig. 4. (continued) disorganization of fibers crossing the septal region. Fimbria: In mutants the enlarged hippocampal fimbria (fi) is shifted rostrally and exhibits a much thicker and less curved fiber structure as demonstrated by region-to-region fiber tracking (*bottom*). cing = cingulum; fx = fornix. Directional color code: *red* = left–right, *blue* = rostral–caudal, *green* = anterior–posterior. Reproduced with permission by Oxford University Press (Ref. (37)). (**b**) A coronal (*left*) and sagittal (*right*) view of the fractional anisotropy map in a fixed mouse brain. A 3D diffusion-weighted fast spin-echo sequence was used with an echo train length of 6 with a TR of 325 ms, first TE of 30 ms, and a TE of 6 ms for the remaining five echoes, ten averages, field of view 14 × 14 × 25 mm^3 and a matrix size of 120 × 120 × 214 yielding an image with (117 μm)^3 voxels. For the calculation, one b = 0 s/mm^2 image (with minimal diffusion weighting) and six high b-value images (b = 1956 s/mm^2) in six different directions [(1,1,0),(1,0,1),(0,1,1),(–1,1,0),(–1,0,1),(0,1,–1)] (Gx,Gy,Gz) were produced. Total imaging time was ~16 h. *Yellows* indicate values closer to unity (fibers are very ordered in one direction) and *deep purples* indicate more isotropy. Figure provided courtesy of Dr Jacob Ellegood.

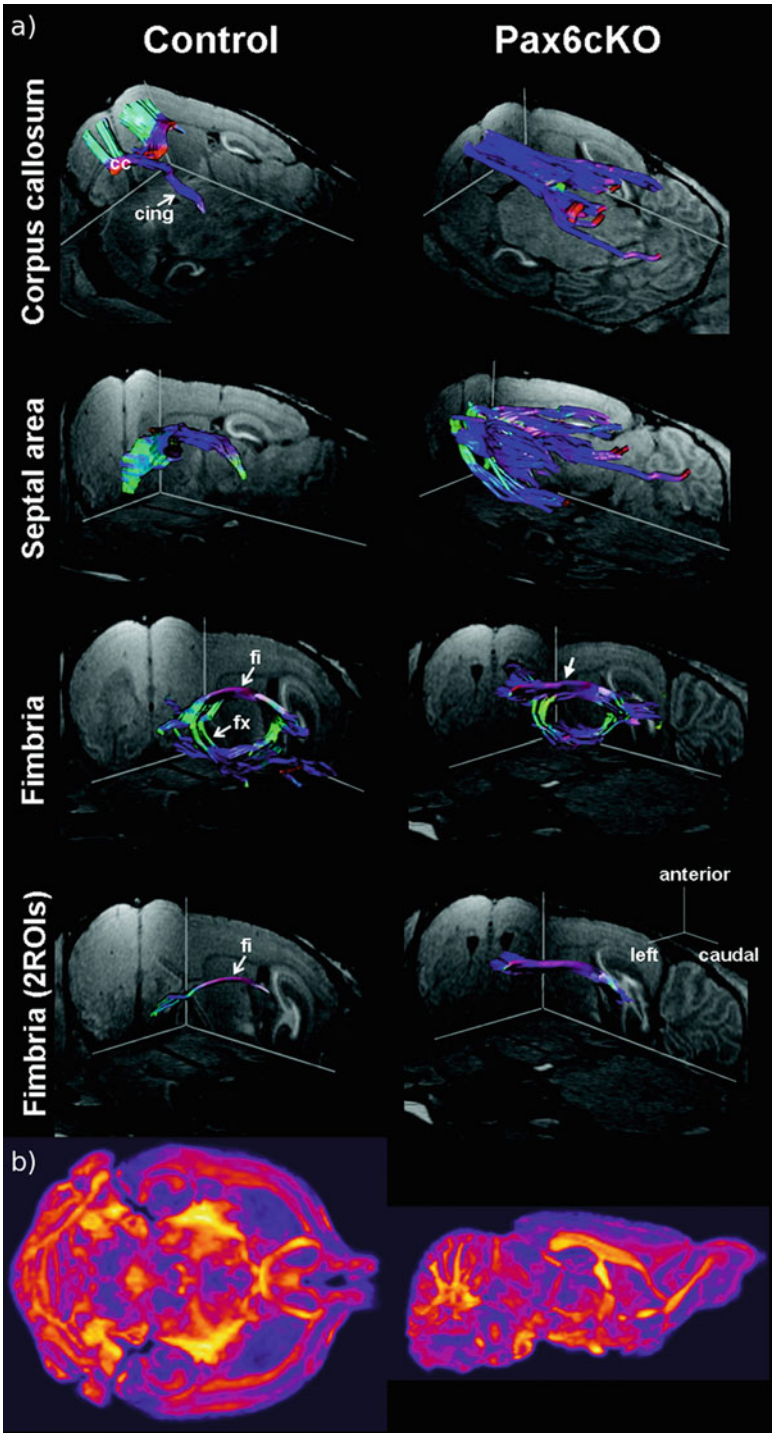

Fig. 4. Applications of diffusion-weighted imaging in mouse brain. For color figures, please refer to the on-line version, which is available through most institutional subscriptions. (**a**) 3D views of major fiber pathways of a control and Pax6cKO mouse in vivo. Corpus callosum: Although controls present with a pronounced connection of the 2 hemispheres via the corpus callosum (cc) and projections into the cingulate and motor cortex, mutants reveal a strong rostrocaudal fiber orientation and a nearly complete lack of interhemispheric projections. Septal area: Mutants are characterized by a vast

2. In most of the chest and abdomen, however, motion is pronounced and cannot be eliminated. Instead, imaging approaches aim to achieve a "snapshot" of the motion. This is particularly challenging as the murine heart rate is typically around 500 beats per minute and the anesthetized mouse breathes once every 1–2 s. In the past decade, several techniques have emerged to enable cardiac cine-MRI in which the ventricular size and shape can be assessed at multiple phases of the heart cycle and is discussed in much greater detail in the **Chapters 20**, **21**, and **22**.
3. Briefly, there are typically two ways of taking images: prospectively and retrospectively. In prospective gating, the scanner is set to acquire data only during a specified phase of the heart cycle. This method is quite efficient and provides excellent cardiac images (48–50). In retrospective gating, data are continually acquired and the respiratory and ECG signals are recorded. Data are oversampled (e.g., data for more than one image are acquired) and then sorted according to cardiac phase and respiratory status retrospectively, retaining only data acquired during the quiescent respiratory period and at a specified cardiac phase (51, 52). A key benefit of the retrospective method is that multiple mice can be imaged in this fashion (53).
4. State-of-the-art techniques to date yield cardiac images on the order of 100 × 100 μm^2 with slice thicknesses at about 0.5 mm, with some groups achieving isotropic voxels (54, 55). Several disease models have been investigated, including models of myocardial infarction (56), transgenic models (57–59), and ischemia (60).
5. Another challenging area of research is imaging the lungs in the mouse. There are typically two ways of studying the lung: using hyperpolarized inert gases to look at the airspaces (61–63) or enhancing the water signal in the lung parenchyma (64, 65). The technical knowledge and skills for set up of a hyperpolarized gas system can be significant, but the reward is images of the airspaces exclusively (*see* **Chapters 10** and **24** for more details). Imaging the proton signal is also challenging as the microstructure of the parenchyma causes T_2^* to be on the order of milliseconds. The T_1 can be shortened by adding a gadolinium-based contrast agent (66) or having the mouse breathe in oxygen (65). This way signal averaging can be applied along with cardiac gating to yield images of the parenchyma (*see* **Fig. 5** from Watt et al.). The highest resolution images are 87 × 87 μm^2 in-plane (66) and a number of disease models in the mouse have been studied including lung cancer (67–69), lung inflammation (61, 70), and cystic fibrosis (64).

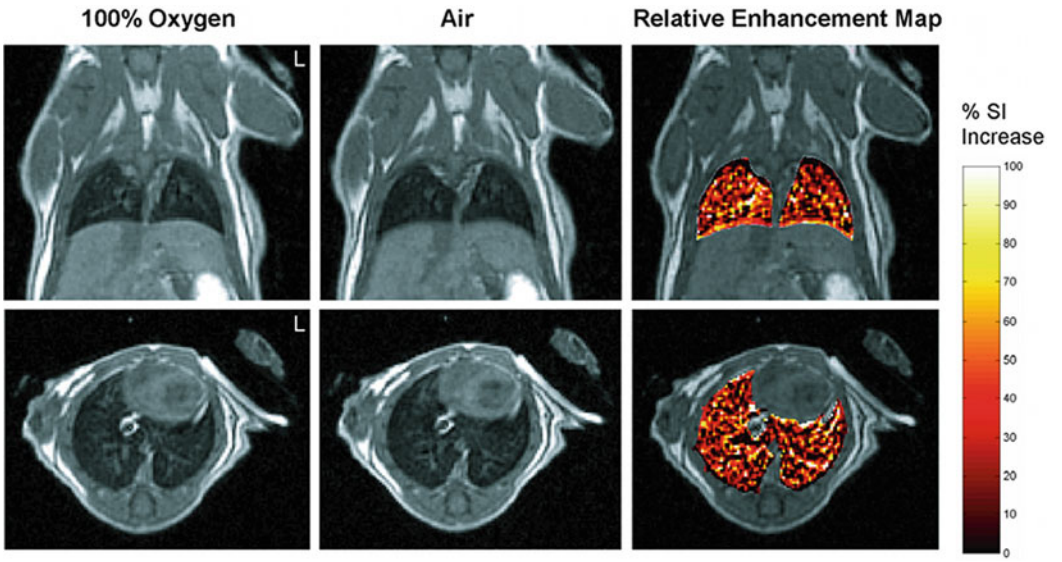

Fig. 5. Oxygen-enhanced images of a normal mouse breathing 100% oxygen and air. For color figures, please refer to the on-line version, which is available through most institutional subscriptions. Coronal (*top*) and axial (*bottom*) images were acquired using a three-dimensional (3D) fast spin-echo (FSE) cardiac-triggered, respiratory-gated sequence with dummy scans. The relative enhancement map shows the percent increase of signal intensity in the lungs observed with 100% oxygen inhalation relative to air for images at the same slice position. To highlight signal enhancement in the lung, the intensity changes in the rest of the body have been masked. All coronal images are shown at a position dorsal from the heart and away from major vessels. Reproduced with permission from Watt et al. (Ref. (65)).

3.3.3. Contrast Agent Administration

It is beneficial in some phenotyping applications to highlight anatomy or function by administration of contrast agents that shorten the T_1 or T_2 relaxation times, producing respectively a bright (positive contrast) or dark (negative contrast) signal. There are a number of classes of contrast agents that can be used with the aim of highlighting vasculature, elucidating tumor boundaries, assessing neuronal function, or even targeting or tracking cells. These are discussed more extensively in other chapters so we discuss them only briefly here.

1. Vascular imaging, although possible with simple pulse sequence selection (**Fig. 6a**), can benefit from administration of contrast agents, including chelated gadolinium (Gd) complexes and iron oxide agents. Functional information can be achieved by assessing blood inflow immediately following injection of contrast agent through a vein and then imaging dynamic changes in image contrast as the agent perfuses through the system (27, 28).
2. Alternatively, injection of agents that remain in the blood pool for extended periods can be used to acquire higher resolution anatomical images of both arteries and veins as well as vascular pathologies such as atherosclerosis (71, 72) (*see* **Fig. 6b–d**).

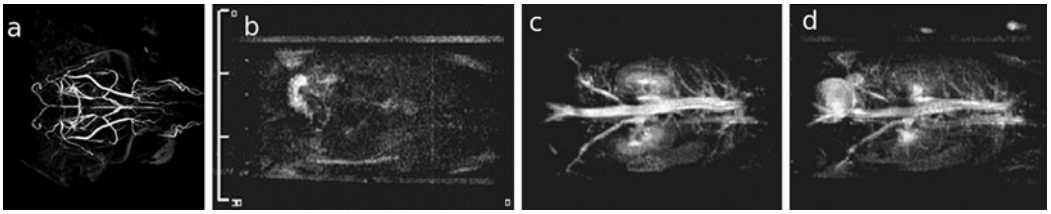

Fig. 6. Different strategies to image the vascular system. (**a**) A horizontal MIP image of the adult mouse brain achieved with an inversion recovery-prepared rapid gradient echo sequence, in which the inversion time was selected to null the tissue signal and highlight blood inflow. Sequence parameters: FOV = 25.6 × 25.6 × 13.6 mm, resolution of (100 μm)^3, TR = 2 s, TE = 2.9 ms, TI = 620 ms, six averages, 64 acquisitions per TR each with 12° excitation spaced 10 ms apart, total acquisition time = 1 h 49 min. **Panels b–d**: 3D magnetic resonance angiography (MRA) before (l) and at 4 (m) and 55 min (n) after contrast injection. With kind permission from Springer Science+Business Media: MAGMA, Contrast enhancement in atherosclerosis development in a mouse model: in vivo results at 2 Tesla, 17, 2004, 191, L Chaabane et al., part of **Fig. 1** (Ref. (120)).

3. Assessment of functional perfusion or microvasculature parameters based on pre- and post-injection image evaluation is also being explored (73–77). Administration of vascular agents is most easily performed via intravenous tail vein injections, although alternative routes are necessary for rapid bolus injections.
4. Neuronal function may, in some cases, be explored via administration of Mn. An intrapertioneal injection of Mn followed by a period in which mice are exposed to stimulus can modify the uptake of Mn sufficiently to show functional differences between different stimulus conditions. This has been demonstrated most clearly in the auditory system (78, 79). Focal injections of Mn or exposure of the olfactory system to Mn can also provide measurements of axonal transport and regional activity (29, 80, 81) with sufficient sensitivity to show differences in transgenic mice (82).

Significant effort continues in the development of molecular imaging, which in MRI includes applications of cell tracking, localization of targeted contrast agents, or imaging of gene expression. Successful development in this area will produce new and important in vivo phenotyping opportunities. Several genetic agents, which produce or accumulate contrast via expression of a transgene, are being explored with the hope of elucidating spatial and temporal gene expression profiles in development or disease (83–89). Alternatively, agents designed to label particular cell populations by uptake or binding to specific surface markers are also in development. Current applications in molecular imaging include detection of transgene expression in tumor-bearing mice (88, 90), integrin expression in artherosclerotic plaques (91, 92), and finding specific peptides that will attach to amyloid plaques (93) or inflammatory lesions (94). The tracking of both injected (95–99) and endogenous (31–33) cell populations after labeling

with iron oxide agents shows some promise, permitting the evaluation of cellular migration behaviors in vivo during homeostasis or disease. The potential impact of genetic and cellular imaging is remarkable, motivating needed developments of these MRI methods in molecular imaging.

3.3.4. Postmortem Imaging

In vivo imaging is an extremely useful aspect of MRI. However, some studies are best served by increasing scan time to achieve microscopic resolutions in ex vivo specimens. Since the scan times can approach tens of hours, it is necessary to fix tissue to avoid degradation.

1. To image individual organs like the brain, kidneys, and liver, the mouse is first fixed by conventional perfusion. In this procedure, mice are first anesthetized (e.g., by ketamine/xylazine) and then placed in a supine position.
2. A midline incision through the chest is followed by catheterization of the left ventricle. A cut is also made in the right atrium and then a saline/heparin flush is followed by perfusion of a fixative solution.
3. Including a contrast agent such as gadolinium in the perfusates also serves to reduce subsequent imaging time.
4. The organ of interest is then excised, immersed in a proton-free, susceptibility-matching fluid and then imaged.
5. Smaller, solenoidal RF coils can be used when imaging excised organs, which give better sensitivity.
6. In the case of embryos, they are removed from the mother and then immersion-fixed in formalin and 4 mM Multi-Hance (Bracco Diagnostics Inc, Princeton, NJ) for 3 days and then transferred to 1% agarose. **Figure 7** shows an example of a 15.5-dpc (days post coitum) embryo imaged in this fashion.

To image the whole mouse adult body, it is desirable to avoid damage to the thoracic cavity and two techniques have emerged to perfusion fix the mouse without breaching the chest cavity.

1. One method involves cannulating the right jugular vein and the left carotid artery and passing the perfusates through these points (100).
2. The other uses an ultrasound biomicroscope to guide the catheter into the left ventricle, allowing the mouse to be fixed in much the same fashion as the open-heart perfusion fixation, with the exception that the perfusates are drained through cuts in the femoral and jugular veins (101). **Figure 2a** shows an MR image of a mouse fixed in such a fashion.

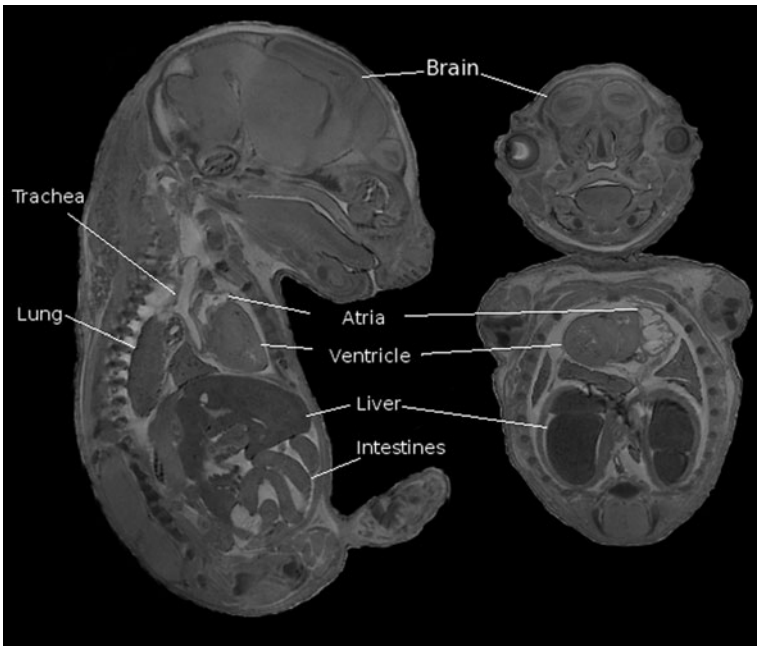

Fig. 7. Sagittal (*left*) and coronal views of a 15.5-dpc mouse embryo. A gradient echo scan was used with the following scan parameters: TR/TE =50/5.06 ms, flip angle 60°, FOV = 2.5 × 1.4 × 14 cm, resolution is $(32\ \mu m)^3$, six averages for a total scan time of about 14 h.

3.4. Anatomical Image Analysis

Figure 8 shows several examples of different phenotyping analyses for MRI that will be discussed below, as applied to neuroanatomical mutants (reproduced from Nieman et al. (21)). Briefly, the panels (a) and (b) show significant local volume changes; panels (c) and (d) show two illustrations in which a phenotype is immediately recognizable by eye; panels (e) and (f) are more subtle mutant phenotypes which require detailed statistical analyses for identification.

3.4.1. Basic Quantitative Measures

After acquiring image data for a study, the main challenge is quantitative data analysis. A human observer can make qualitative observations (e.g., "the left ventricular wall is thicker than the wildtype" or "the tumor looks bigger in one mouse compared to another") but the real power of MRI is that quantitative measures can be obtained from the images.

Fig. 8. (continued) (f) for the respective overlays. Data were acquired with in vivo magnetic resonance imaging (MRI) (panels a, d, and e), ex vivo specimen computed tomography (c), ex vivo specimen MRI (d), and in situ specimen MRI (f). All MRI images are single slices from three-dimensional isotropic datasets. Reproduced with permission from Nieman et al. (Ref. (21)).

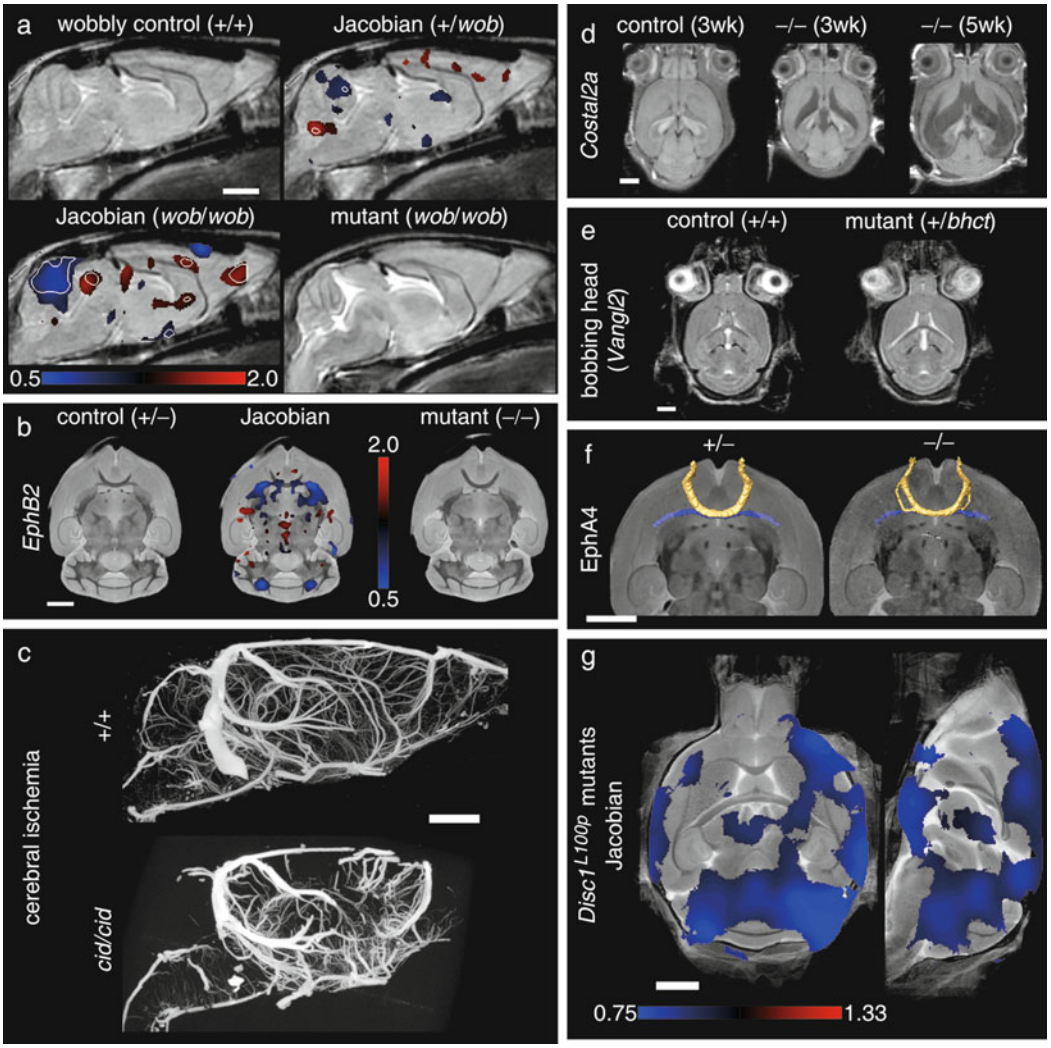

Fig. 8. Neuroimaging findings in mouse mutants. For color figures, please refer to the on-line version, which is available through most institutional subscriptions. In (**a**), an average control mouse image is shown with two Jacobian overlays indicating local volume changes in the heterozygous and homozygous wobbly mutants. Values greater or less than 1 in the Jacobian field represent growth or shrinkage, respectively. Jacobian overlays in panel (a) are shown in regions where $p < 0.05$ with white contour lines indicating $p = 0.002$ (a false discovery rate of 5% in the homozygous mutant). The average homozygous wobbly mutant image is also shown for reference and exhibits a small cerebellum. In (**b**), data from the EphB2 knockout study indicates an abnormality at the anterior commissure (the posterior portion is absent). Jacobian data in the middle image indicate regions where $p < 0.003$ (5% false discovery rate). Panel (**c**) shows two sample micro-CT datasets as maximum intensity projections. The cerebral ischemia mutant shows a striking defect in vascular perfusion as compared to the control. Panels (**d**) and (**e**) provide two examples of hydrocephalus. Three different individual images from the sonic hedgehog pathway mutation are shown (d) with massive expansion of the ventricles (shown as hypo-intense regions). In panel (e), control and mutant averages from the bobbing head study show more subtle ventricle expansion (shown as hyper-intense regions). In this case, statistical comparison of the mutant Jacobian values to a set of 20 control mice (four wildtype littermates supplemented with non-littermate wildtypes) shows expanded ventricles (regions indicate a 5% false discovery rate) and increased variability at the lateral ventricles (Jacobian variance ratio is shown in regions where $p < 0.05$). In the final panel (**f**), regions of abnormality representative of the disrupted-in-schizophrenia-1 mutants (Disc1) are shown as Jacobian data overlaid on an average image (regions indicate $p < 0.05$ by a Mann–Whitney U test). All white scale bars indicate 2 mm. Color scales are indicated in panels (a), (b), (e), and

1. Using freely available image processing packages, the previous examples can easily be quantified by measuring the wall thicknesses and segmenting tumor volumes. Most visualization packages have a manual segmentation feature and many have some form of semi-automatic segmentation.
2. If the subject numbers are few, manual segmentation is rapid, reliable, and widely utilized (7, 46, 51). An advantage is that it does not require any knowledge or development of more elaborate image processing methods. **Figure 9** shows an example of manual labeling of 62 substructures in the mouse brain (102).
3. Typically small, simple structures (e.g., the anterior commissure in the brain) can be segmented in tens of minutes as they only occupy a few slices within a dataset.
4. Segmenting more expansive structures like the corpus callosum or hippocampus can take more than an hour. If many mice are part of the study, manual segmentation on all subjects is prohibitive; hence using computer-aided image processing tools is prudent.

3.4.2. Registration

It is frequently impractical to perform manual segmentation of volumes for image analysis, and, in these cases, it is common to make use of registration algorithms to elucidate any disparities. The registration process produces transformed images that are aligned with one another such that common structures are placed on top of one another, in "register." The image transformations required to achieve such alignment encode phenotypic differences. The phenotypes can be extracted from registration-based analyses in several ways, based on structural volumes as described above or on more sophisticated voxel-by-voxel measurements of shape or size differences.

1. A number of registration packages are listed in **Section 2.5**, item 3. In general, the registration process begins by first globally aligning images through affine registration, which includes global translations, rotations, scales, and shears. These modifications are considered linear operations and are applied to the entire image (*see* **Note 8**).
2. With all images in this orientation, it is convenient to average the intensity images to produce a representative average image. This scaled average accounts for overall size and shear distortion differences. Although this average image space may be defined by a reference image, it is more satisfying to define an unbiased space incorporating all images under analysis as described in detail elsewhere (103).
3. The initial average after affine registration is generally fairly "blurred," due to imperfect alignment of anatomical features. An iterative nonlinear registration process can refine

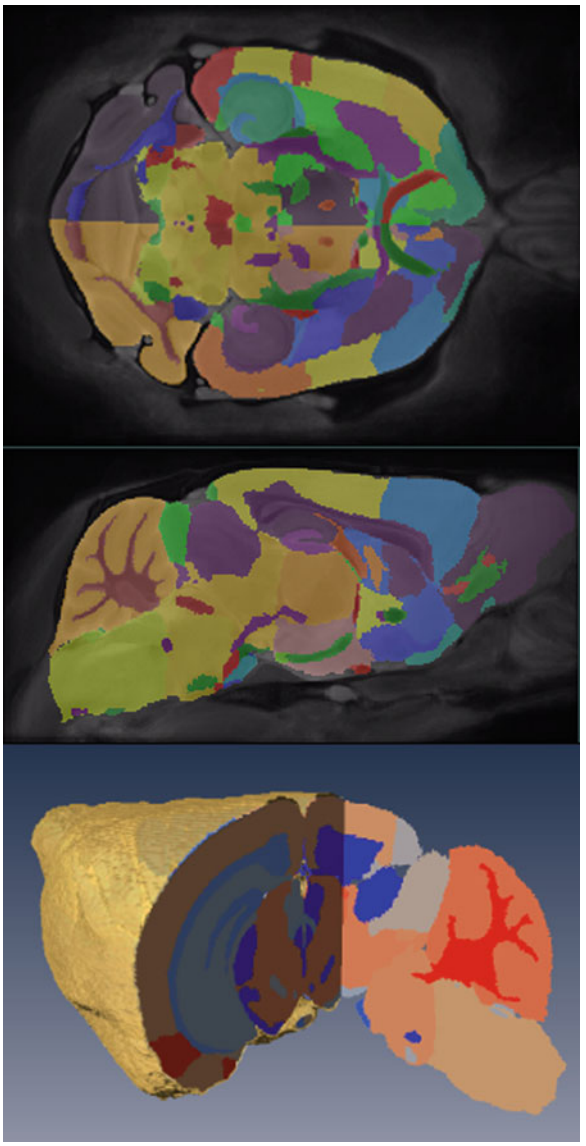

Fig. 9. Three views from a manual segmentation of 62 sub-structures from an average of 40 mouse brains (Ref. (102)). For color figures, please refer to the on-line version, which is available through most institutional subscriptions. The brains were from 20 male and 20 female 12-week-old C57Bl/6 J mice. Three brains were imaged in parallel with a fast spin echo sequence (TR/TE = 325/32 ms, four averages, $(32\ \mu m)^3$ resolution for a total scan time of 11.3 h. The *top* and *middle* panels show coronal and sagittal slices (respectively) of the atlas overlaid on top of the average. The *bottom* panel is a 3D volume rendering with a cutout showing the segmentation (a different colormap was used than the previous two panels).

the average and bring the component images into improved alignment. In this step, local regions of the image are shifted to match features with a target image (this could be a chosen representative image or the calculated average of the population (103)).

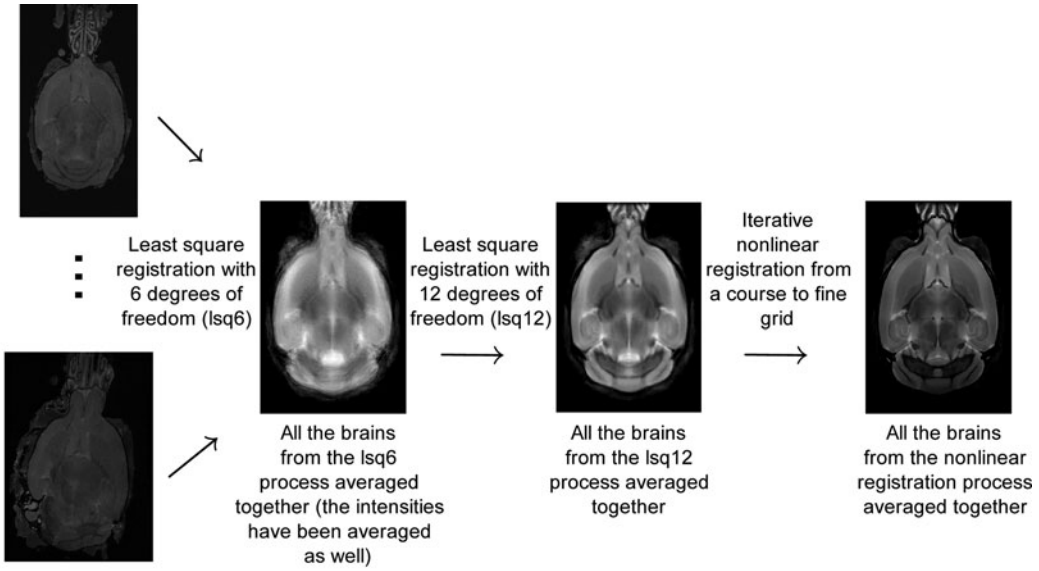

Fig. 10. The registration pipeline used at the Mouse Imaging Centre. This pipeline has been applied to fixed brains (Refs. (22, 102, 104)), live brains (Refs. (121, 122)), and embryos (unpublished).

4. The nonlinear registration is performed iteratively using a coarse-to-fine approach, with a gradual decrease of grid-point spacing (i.e., increasing registration resolution) until the desired level of refinement is achieved. **Figure 10** shows a sample registration pipeline.
5. The simplest way to see if a registration was successful is to visually verify the alignment of all images. If there are anomalies, then it could be that the registration procedure needs to be adjusted (*see* **Note 9**) or that artifacts in particular images are problematic. In some cases, however, it is actually very difficult to register two subjects together if the images are too dissimilar, for example, in **Fig. 8d**, the ventricles between the different genotypes are so different that the structures should be considered nonhomologous, a violation of assumptions inherent in the registration process. Nonetheless, it is often possible to use registration even in cases of mild nonhomology, as for instance in **Fig. 8b**—the posterior portion of the anterior commissure is absent in the mutant—in which registration was still largely successful.

3.4.3. Volumetrics

By combining manual segmentation with the registration transformations described, it is possible to determine the volumes of structures in many mouse images after segmentation of a single image, greatly improving study throughput (103, 104).

1. The typical procedure that we use is to manually label the average image and then to "back propagate" the segmented labels (which may include 40–60 substructures in the brain) along the transformation prescribed by the registration results.
2. For instance, after segmenting the whole brain in an average image and "back propagating" through the nonlinear and affine registrations to the original images, we measured the whole brain volume in C57/Bl6 mice and determined male brains were 2.5% larger than their female equivalents (22). This method, which uses "unscaled" comparisons of whole brains and cerebral substructures, gives absolute volume values and is preferred for performing survey studies, (i.e., screening genetically mutant mice).
3. An alternative basis for analysis uses volumetrics after affine registration—a "scaled" comparison—which may be more appropriate in some instances, particularly if specific hypotheses are to be tested (105). In this analysis, one compares a normalized or relative structure volume, which may also reveal subtle differences. The most appropriate comparison, based on "unscaled" or "scaled" image data, must be considered carefully.
4. This technique of finding substructural volumes in the brain is very difficult to accomplish histologically—although this remains the gold standard (*see* **Note 10**)—and a comparison between striatal volumes found with MRI and registration versus histology demonstrates the superiority of MRI for volume-based analyses of structure (104). A number of groups are using similar methods to study cerebral structures in various disease models (30, 106, 107).
5. One limitation of volumetric analysis is that it reduces complex shapes down to a single number. This line of inquiry will fail if multiple, opposing volumetric changes occur within a structure, minimizing or eliminating any cumulative volume change. Also, in the case that there is no volume change but rather a positional shift, volumetrics may also fail to detect the change. In this case, more sophisticated analyses are possible using the results of the registration.
6. The results of the registration provide not only a set of transformed images, but also a map encoding these image transformations with vectors or matrices. These maps may be analyzed computationally to look for group differences, without the need to reference segmented structure volumes. The vector representation of the image transforms is frequently referred to as the deformation field.

3.4.4. Analysis of the Deformation Field

Deformation-based analyses compare a metric computed from the deformation field on a per voxel basis, as opposed to reducing an entire image set to some defined number of segmented substructures. Below, we describe metrics to represent (1) positional shifts of anatomy; (2) anatomical variability; (3) volume changes in regions or structures, and (4) other methods to highlight local changes in shape.

1. The most straightforward deformation-field comparison of interest may be the vector difference from an individual to the group average from one genotype group to another.
2. A display of the magnitude of this difference provides a look at the regions of greatest positional shift between subjects and can be graphically displayed. In a set of genotypically identical mice, the set of all such fields can provide a sense of the inherent variability in the image data (22, 108).
3. This variability can be computed on a per voxel basis in a population by computing the arithmetic mean of all displacement vectors (**Fig. 11**) and represents the typical deviation (in millimeters displacement) from the population average.
4. Beyond a simple display of differences in the deformation fields themselves, local volume changes between images or

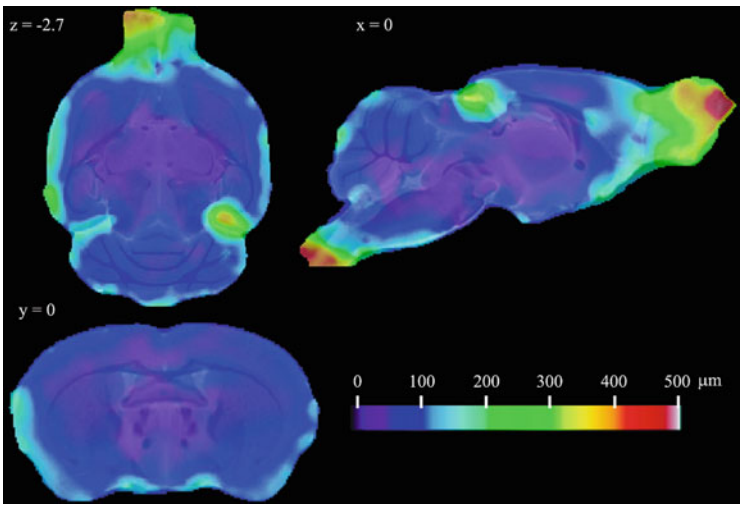

Fig. 11. The mean positional difference image created from the arithmetic mean of the deformation vectors used to create an average of nine excised 129S1/SvImj mouse brains. For color figures, please refer to the on-line version, which is available through most institutional subscriptions. Deformation magnitudes (measured in micrometers and shown in spectral color scale) are overlaid on top of the average image (*in grayscale*). *Purple* and *blue* regions (on the low end of the scale) indicate low variability, while *red* and *white* (on the high end of the scale) indicate high variability. Shown are three orthogonal slices with stereotaxic coordinates given in millimeters. With kind permission from Springer Science+Business Media: Cerebral Cortex, 15, 2004, 642, N Kovacevic et al., **Fig. 4** (Ref. (103)).

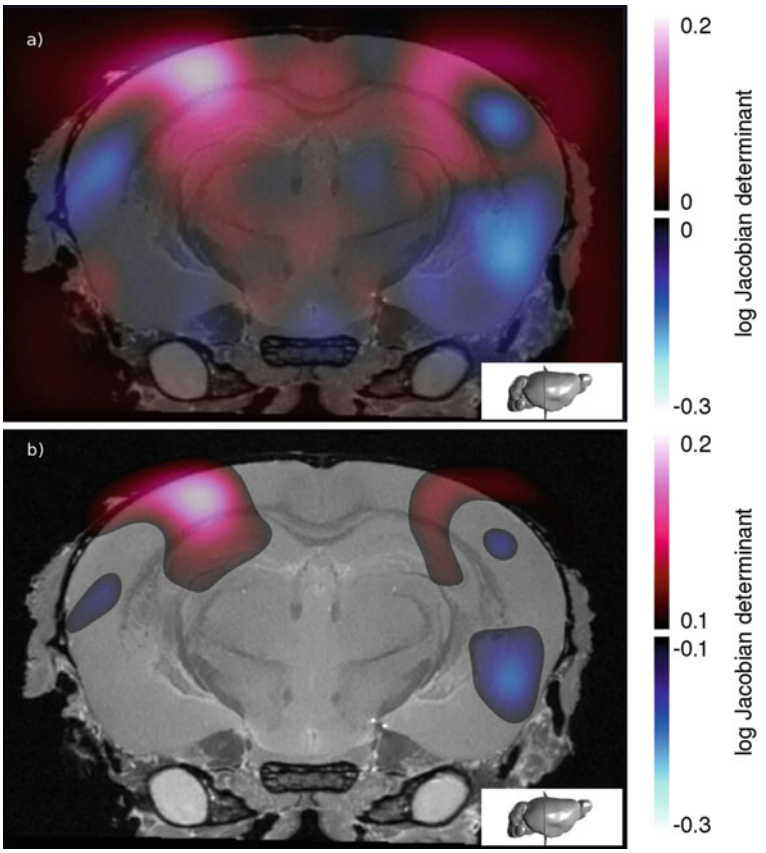

Fig. 12. An example of the log of the Jacobian determinant. For color figures, please refer to the on-line version, which is available through most institutional subscriptions. Using nonlinear image registration, an unbiased group average is created from 10 wild-type and 10 mutant mouse brain MRIs. The Jacobian determinant, calculated from the deformations needed to take each mouse's anatomy into the final group average space, is a measure that illustrates the expansion and contraction of tissue. In the colored areas, the log of the Jacobian determinant of a single wildtype brain is shown, overlaid on the anatomy of that subject resampled to the group average. The areas in *red* (positive scale) indicate areas where this particular brain had to grow to get to the group average, and the areas in *blue* (negative scale) where the brain had to shrink. The coronal level of the section is pictorially illustrated in the *bottom right corner*. (**a**) The full log of the Jacobian is shown and (**b**) the log of the Jacobian is thresholded to show more relevant areas of change. Figure provided courtesy of Matthijs van Eede.

populations can be determined by computing the determinant of the Jacobian matrix, formed by the matrix of deformation-field partial derivatives (*see* **Note 11**) (109). **Figure 12** shows an example image of the log of the Jacobian determinant, usually simply referred to as the Jacobian.

5. In the places where the log Jacobian is equal to 0, there is no local volume differences between groups; a value less than 0 indicates shrinkage and a value greater than 0 indicates

a growth. While valuable information can be gained from the Jacobian determinant, there is additional information encoded in the full Jacobian matrix, including anisotropic volume changes. Ongoing research therefore explores the use of alternative Jacobian-based metrics, such as strain matrices (110), to improve local detection.

6. Combined use of segmented structures and deformation-field measurements are another alternative for analysis. For instance, comparing the surface normal vector of a segmented structure with the local direction of the deformation field can determine local surface displacements. By calculating this vector at every point of a surface, a different metric for shape changes can be quantified (111).

3.4.5. Statistical Considerations

With the exception of gross anatomical phenotypes which are immediately and consistently obvious on simple inspection, it is necessary to isolate regions of significant differences in a statistically rigorous fashion. This is true independent of the metric—such as those in the previous section—selected as a basis for comparison. Cases that necessitate statistical comparison are among the more interesting to study by imaging, as the imaging results are instrumental in phenotyping these models. In studies where a measure of interest can be identified prospectively, such as an anatomical feature's volume, area, thickness, or length, it is beneficial to perform such measurements on each individual image and then compare the measured results. This analysis process has the benefit of condensing the most relevant image information into a single metric at the outset, simplifying statistical comparison to a single groupwise test. As in the comparison of segmented volumes, these measurements can be performed "manually" in each mouse or facilitated by the registration procedure to transfer segmentations and annotations from one image to all others. Thus, after defining the measures of interest in one image, the rest of the dataset can be generated computationally.

It is nevertheless common in imaging studies to be screening for possible phenotypes in a new mouse model, to seek secondary phenotypes in addition to more obvious ones, or to consider substructural features. In these cases, the unbiased nature of a voxel-by-voxel comparison is desirable. Voxel-by-voxel comparisons may be parametric, such as Student's *t*-tests or Hotelling's *T*-squared tests (112, 113), or nonparametric, such as *U* tests (114) or permutation tests (115), and are widely available in scientific or statistical software packages. It is necessary to note in voxel-by-voxel analyses, however, that the process of making many statistical comparisons increases the likelihood of false positives. In fact, given that a high-resolution (fixed, 32 μm isotropic) brain image contains ~18 million voxels, one is assured, using the

customary $p < 0.05$ criterion, of finding incorrectly identifying 5% of them as significant (i.e., 90,000 false-positive voxels!).

For this reason, it is necessary in voxelwise statistical analyses to correct statistical results for multiple comparisons. While this is an area of ongoing research, particularly in neuroimaging applications, several methods have become fairly common. In our own studies, we have most frequently used the false discovery rate (FDR) (*see* **Note 12**), which controls the average proportion of false-positive voxels to true-positive voxels (*see* **Fig. 8a** and **b**). The benefit of the FDR is that it is easy to implement (i.e., also available in many existing software packages as described in **Section 2.5**, item 4), conceptually simple, and has been used quite widely. It is, however, quite conservative in cases where only a small number of voxels are affected and fails to take into account spatial relationships between significant voxels. The latter is particularly unsatisfying in deformation-based morphometry, where the registration procedure inherently constrains neighboring voxels to produce smooth deformations. An alternative method of adjusting statistical thresholds may be based upon treating the features of a statistical map collectively and considering the likelihood of such features occurring in a comparable random map. Such methods based on random field theory are also implemented in various software programs. In a similar spirit, authors have proposed various cluster-based analyses, in which groups of voxels with sufficiently similar responses are treated as a collective. This both increases the signal-to-noise ratio (after forming a score representative of all voxels in the cluster) and reduces the number of statistical comparisons, in part mitigating the multiple-testing problem. For voxelwise statistical tests in large datasets, it is important that one of these methods be employed to ensure reliable results.

Deformation-based analyses with statistical testing are particularly powerful for isolating subtle phenotypes. However, the ability to do so is a function of several factors. Underlying variability, be it biological or methodological (*see* **Note 13**) in nature, naturally masks small phenotypes and it is important to understand the limitations of a given protocol. With this aim, a variability map can be produced to indicate variability inherent in the population and/or method (particularly if specimen preparation is involved). For instance, **Fig. 11** shows a variability map of nine fixed, 129S1/SvImJ mouse brains reproduced from Kovacevic et al. (*see* **Note 14**). The variability in the inner structures of the brain is quite low (less than 120 μm or two voxels in a 60 μm image). If the phenotype involves detection of changes on this order, or the phenotype itself is highly variable (*see* **Note 15**), many more mice will be required. The process of estimating the variability and the number of mice required can be made more formal by specifically finding the "noise" intrinsic to a structure

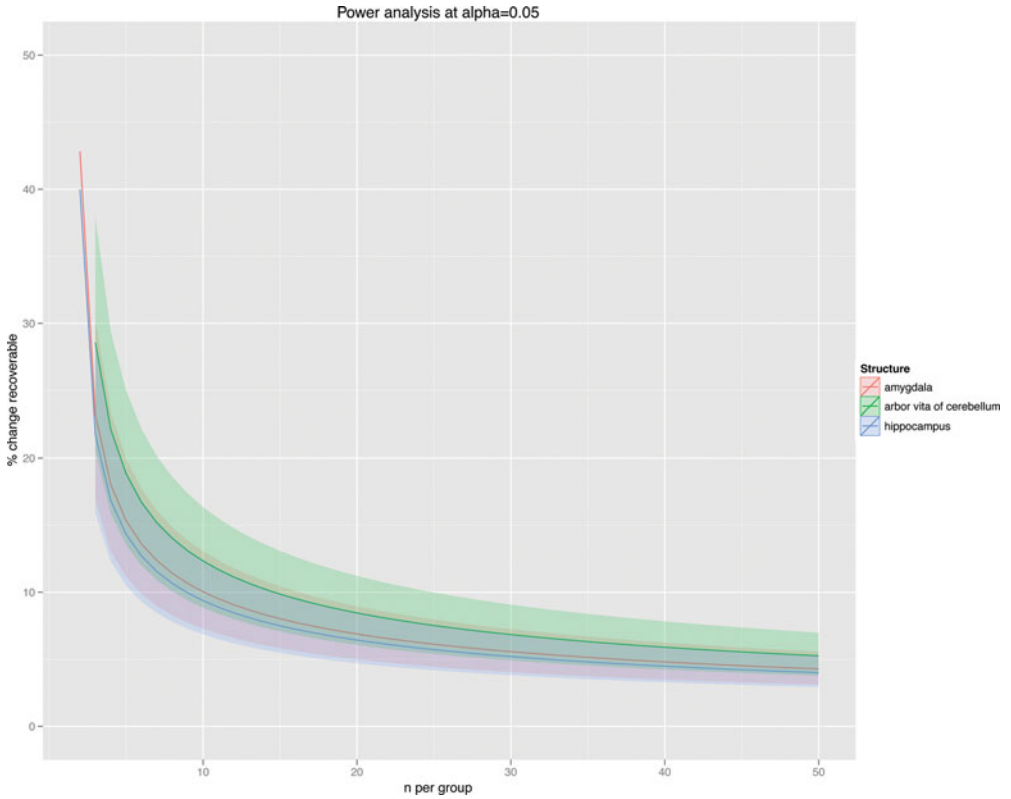

Fig. 13. A graph showing the power analysis at an α of 0.05 calculated from eight groups of wildtype mice (about 150 mice in total) for three structures in the brain: amygdala, arbor vita of the cerebellum, and the hippocampus. For color figures, please refer to the on-line version, which is available through most institutional subscriptions. The *y*-axis shows the expected change given the size of the groups on the *x*-axis. The *top limit* for each structure is the maximum variance, the *solid line* is the mean variance of the groups and the *bottom limit* is the minimum variance. As an example, if you expect that the volume difference in the arbor vita of your mutant population is about 20%, then you would need 9–10 mice per group to find a significant difference with $p < 0.05$. This graph quantitatively shows that more subtle differences require more animals per group. Figure provided courtesy of Dr Jason Lerch.

in question. As an example, Lerch and colleagues measured the mean and standard deviation of the cortical thickness in a group of 20 mice (116). From this, they created a power analysis graph that indicated 6–9 mice per group were sufficient to result in statistically significant results in their study. In **Fig. 13**, we have recreated a similar power analysis graph based on about eight groups of wildtype controls from different experiments; each group had between 7 and 20 mice. Within each group the variance in volumes was computed and the across-group comparisons were used to generate the group. Such information provides helpful guidelines for planning mouse-phenotyping studies.

3.5. Conclusions

In this chapter, we have described the techniques, tricks, and experiences we have gained over the last decade as a research group devoted to mouse imaging. During this period, the number

of groups performing mouse MRI has continued to increase, each of these adding their own various implementations and techniques. We also listed some of the more obvious pitfalls that may be encountered by someone breaking into this exciting field of research. The live imaging is perhaps the most alluring aspect of mouse MRI, achieving isotropic resolutions of ~100 μm and permitting longitudinal evaluation. In some investigations, however, higher impact data may be acquired by preparing ex vivo samples, to achieve isotropic resolutions of less than 40 μm. While many measures of phenotype are possible using various quantitative and functional MRI methods, detection of anatomical changes remains a common and particularly powerful approach. Careful preparations and imaging methods permit computer-aided detection of anatomical phenotypes, making this method appropriate for high-throughput analyses of mutant mice. In this regard, MR-based mouse phenotyping stands to contribute a great deal to the understanding of the genetic basis of human diseases and the subsequent exploration of novel therapies.

4. Notes

1. The most significant benefit of noninvasive imaging is evaluation of temporal and spatial evolution of disease in individual mice. This increases statistical power because it eliminates heterogeneities that exist between mice. A good example is that of genetically engineered tumor models, in which time and location of tumor onset can vary from one mouse to the next. However, imaging protocols in compromised mice—young, old, or mutant—need to be judiciously chosen, as mice may be too fragile to survive long scan durations or frequently repeated sessions.
2. The biggest confounding factors in live imaging are motion artifacts. Because an image can take anywhere from a minute up to several hours, physiological motion or postural changes will compromise imaging results. In our lab, we have devised a custom-built, molded sled (**Fig. 1**) (36). The mouse lies prone on the sled and its head can be held in place for neuroimaging using Velcro straps. The sled also incorporates embedded ECG, respiratory, and temperature monitoring devices, greatly simplifying animal setup.
3. Injectable anesthetics (e.g., ketamine/xylazine, Avertin) can also be used, eliminating the need for gaseous delivery and scavenging hardware. However, these are only useful for short imaging sessions as the anesthetic wears off in 30–45 min. While it is possible, in principle, to deliver

anesthesia via a catheter in the tail vein during the imaging session, this adds a significant level of complication and is not recommended.

4. The amount of anesthesia and maintenance temperature will change with other strains of mice, which may metabolize anesthetic at different rates.
5. A water bath may be undesirable in some applications because it needs to be in close proximity to the mouse. This may necessitate a larger volume coil, which results in reduced SNR if the coil is used for both transmit and receive. If a small, localized surface coil is used then a water bath should have no impact on SNR if it can be positioned away from the receive coil (but still close to the mouse).
6. The ECG connections routinely show a respiratory signal superimposed with the cardiac signal. The two signals can, in principle, be separated electronically to provide separate cardiac and respiratory traces for monitoring and triggering. However, in practice, a "cleaner" respiratory signal is produced by a respiratory bellows or pillow system.
7. All vendors' platforms will perform standard image acquisitions and reconstructions automatically. However, for many sequences—particularly, specialized ones—it may be necessary or beneficial to implement site-specific image sequences and/or perform off-line reconstruction to ensure all acquisition and processing steps are understood and optimized.
8. It is in this step that it becomes obvious if the care in preplanning of mouse positioning was sufficient. If different mice were not imaged in roughly similar positions, initial registration-based alignment will fail and some manual alignment will be necessary.
9. Troubleshooting a registration pipeline is methodical work. There are images produced at each step along the way and careful inspection of these images will reveal where in the pipeline a failure occurred. The parameters leading up to that step need to be tweaked. Examples of adjustments that can push along the pipeline include decreasing step sizes or increasing blurring of the input images.
10. Using MRI in biomedical research can be extremely powerful as samples can undergo subsequent histological verification. This is the gold standard in which a tissue is sectioned into a thin slice and studied with light microscopy, and remains a necessity to confirm mouse MRI results. A whole battery of histological stains further enhances the ability to highlight different microscopic structures. For example, if MR images indicate that plaques are seen in an Alzheimer's

mouse model, the iron and β-amyloid content can be verified with a Perl's Prussian Blue stain and then a thioflavin-S stain (117). The ability to do histology on mouse models frequently acts as a bridge between preclinical research and clinical diagnostic data.

11. The Jacobian matrix is the matrix of all first-order partial derivatives of a vector-valued function; in this case, the deformation field. Working with the Jacobian is a way of finding and displaying differences between deformation fields.
12. The false discovery threshold (q) is usually set at 0.05, although this seems largely guided by customary use of $p = 0.05$. Some authors have noted that a high q-value (i.e., 0.10) may be appropriate in some imaging experiments, although a strict convention is lacking.
13. If part of the experimental plan is to use registration as the tool for phenotyping, some thought needs to go into what signal-to-noise ratio (SNR) and resolution to use in the images. These are competing factors that must be traded-off with one another in determining how to spend imaging time. A recent study has determined that for the purposes of image registration, the best compromise is achieved by acquiring images with SNR ~20 and "spending" the rest of the time on resolution (118).
14. This particular example was done with mouse brains excised from the skull. Because the brain is very malleable, the variability shown is really more a map of specimen preparation—the regions of highest variability are at the exterior edges and the olfactory bulbs and brain stem. This again emphasizes how important sample preparation—live or fixed—is critical to computer-aided phenotyping. Our subsequent work after this study uses mouse brains in the skull.
15. In some cases, we have seen variable phenotypes especially with conditional knock-outs. This is when the at least two types of phenotype are seen with the same genotype. So sometimes even higher numbers are required to make sure all phenotypes are significantly represented.

Acknowledgments

The authors would like to thank the staff and students of the Mouse Imaging Centre, especially Jun Dazai, Dr Jacob Ellegood, Dr Jason Lerch, Christine Laliberte, Matthijs van Eede, and

Michael Wong for providing figures. The Mouse Imaging Centre (MICe) acknowledges funding from the Canada Foundation for Innovation and the Ontario Innovation Trust for providing facilities along with The Hospital for Sick Children. Operating funds from the Burroughs Wellcome Fund, the Canadian Institutes of Health Research, the National Cancer Institute of Canada—Terry Fox Program Projects, the National Institutes of Health, and the Ontario Research and Development Challenge Fund are gratefully acknowledged. The embryo work was funded by Genome Canada through the Ontario Genomics Institute (2008-OGI-TD-03).

References

1. Lauterbur P. C. (1974) Magnetic resonance zeugmatography. *Pure App Chem* **40**, 149–57.
2. Clapham J. C., Arch J. R. S., Chapman H., et al. (2000) Mice overexpressing human uncoupling protein-3 in skeletal muscle are hyperphagic and lean. *Nature* **406**, 415–8.
3. Jalanko A., Tenhunen K., McKinney C. E., et al. (1998) Mice with an aspartylglucosaminuria mutation similar to humans replicate the pathophysiology in patients. *Hum Mol Gen* **7**, 265–72.
4. Jones M. E., Thorburn A. W., Britt K. L., et al. (2000) Aromatase-deficient (ArKO) mice have a phenotype of increased adiposity. *PNAS* **97**, 12735–40.
5. Bock N. A., Zadeh G., Davidson L. M., et al. (2003) High-resolution longitudinal screening with magnetic resonance imaging in a murine brain cancer model. *Neoplasia* **5**, 546–54.
6. Fomchenko E. I. and Holland E. C. (2006) Mouse models of brain tumors and their applications in preclinical trials. *Clin Cancer Res* **12**, 5288–97.
7. McDaniel B., Sheng H., Warner D. S., Hedlund L. W., and Benveniste H. (2001) Tracking brain volume changes in C57BL/6 J and ApoE-deficient mice in a model of neurodegeneration: a 5-week longitudinal micro-MRI study. *NeuroImage* **14**, 1244–55.
8. Wei Q., Clarke L., Scheidenhelm D. K., et al. (2006) High-grade glioma formation results from postnatal pten loss or mutant epidermal growth factor receptor expression in a transgenic mouse glioma model. *Cancer Res* **66**, 7429–37.
9. Duhamel G., Callot V., Decherchi P., et al. (2009) Mouse lumbar and cervical spinal cord blood flow measurements by arterial spin labeling: sensitivity optimization and first application. *Magn Reson Med* **62**, 430–9.
10. Hillman G. G., Singh-Gupta V., Zhang H., et al. (2009) DCE-MRI of vascular changes induced by sunitinib in papillary renal cell carcinoma xenograft tumors. *Neoplasia* **11**, 910–20.
11. Berry C. J., Miller J. D., McGroary K., et al. (2009) Biventricular adaptation to volume overload in mice with aortic regurgitation. *J Cardiovas Magn Reson* **11**, 27.
12. Smits A. M., Van Laake L. W., Den Ouden K., et al. (2009) Human cardiomyocyte progenitor cell transplantation preserves long-term function of the infarcted mouse myocardium. *Cardiovas Res* **83**, 527–35.
13. Greve J. M., Williams S. P., Bernstein L. J., et al. (2008) Reactive hyperemia and BOLD MRI demonstrate that VEGF inhibition, age, and atherosclerosis adversely affect functional recovery in a murine model of peripheral artery disease. *J Magn Reson Imaging* **28**, 996–1004.
14. Schneider J. T. and Faber C. (2008) BOLD imaging in the mouse brain using a turboCRAZED sequence at high magnetic fields. *Magn Reson Med* **60**, 850–9.
15. Mori S. and Zhang J. (2006) Principles of diffusion tensor imaging and its applications to basic neuroscience research. *Neuron* **51**, 527–39.
16. McCreary C. R., Bjarnason T. A., Skihar V., Mitchell J. R., Yong V. W., and Dunn J. F. (2009) Multiexponential T_2 and magnetization transfer MRI of demyelination and remyelination in murine spinal cord. *NeuroImage* **45**, 1173–82.
17. Stanisz G. J., Odrobina E. E., Pun J., et al. (2005) T_1, T_2 relaxation and magnetization transfer in tissue at 3T. *Magn Reson Med* **54**, 507–12.

18. Luo F., Seifert T. R., Edalji R., et al. (2008) Non-invasive characterization of Beta-amyloid 1–40 vasoactivity by functional magnetic resonance imaging in mice. *Neuroscience* **155**, 263–9.
19. Heerschap A., Kan H. E., Nabuurs C. I. H. C., Renema W. K., Isbrandt D., and Wieringa B. (2007) In vivo magnetic resonance spectroscopy of transgenic mice with altered expression of guanidinoacetate methyltransferase and creatine kinase isoenzymes. *Sub-cell Biochem* **46**, 119–48.
20. Albers M. J., Bok R., Chen A. P., et al. (2008) Hyperpolarized ^{13}C lactate, pyruvate, and alanine: noninvasive biomarkers for prostate cancer detection and grading. *Cancer Res* **68**, 8607–15.
21. Nieman B. J., Lerch J. P., Bock N. A., Chen X. J., Sled J. G., and Henkelman R. M. (2007) Mouse behavioral mutants have neuroimaging abnormalities. *Hum. Brain Mapp* **28**, 567–75.
22. Spring S., Lerch J. P., and Henkelman R. M. (2007) Sexual dimorphism revealed in the structure of the mouse brain using three-dimensional magnetic resonance imaging. *NeuroImage* **35**, 1424–33.
23. Bock N. A., Nieman B. J., Bishop J. B., and Henkelman R. M. (2005) In vivo multiple-mouse MRI at 7 Tesla. *Magn Reson Med* **54**, 1311–6.
24. Brockmann M.-A., Giese A., Ulmer S., et al. (2006) Analysis of mouse brain using a clinical 1.5 T scanner and a standard small loop surface coil. *Brain Res* **1068**, 138–42.
25. Chronik B., Alejski A., and Rutt B. K. (2000) Design and fabrication of a three-axis multilayer gradient coil for magnetic resonance microscopy of mice. *Magma* **10**, 131–46.
26. Brau A. C. S., Wheeler C. T., Hedlund L. W., and Johnson G. A. (2002) Fiber-optic stethoscope: a cardiac monitoring and gating system for magnetic resonance microscopy. *Magn Reson Med* **47**, 314–21.
27. Herold V., Parczyk M., Mörchel P., et al. (2009) In vivo measurement of local aortic pulse-wave velocity in mice with MR microscopy at 17.6 Tesla. *Magn Reson Med* **61**, 1293–9.
28. Parzy E., Miraux S., Franconi J.-M., and Thiaudière E. (2009) In vivo quantification of blood velocity in mouse carotid and pulmonary arteries by ECG-triggered 3D time-resolved magnetic resonance angiography. *NMR Biomed* **22**, 532–7.
29. Pautler R. G., Silva A. C., and Koretsky A. P. (1998) In vivo neuronal tract tracing using manganese-enhanced magnetic resonance imaging. *Magn Reson Med* **40**, 740–8.
30. Bock N. A., Kovacevic N., Lipina T. V., Roder J. C., Ackerman S. L., and Henkelman R. M. (2006) In vivo magnetic resonance imaging and semiautomated image analysis extend the brain phenotype for cdf/cdf mice. *J Neurosci* **26**, 4455–9.
31. Shapiro E. M., Sharer K., Skrtic S., and Koretsky A. P. (2006) In vivo detection of single cells by MRI. *Magn Reson Med* **55**, 242–9.
32. Sumner J. P., Shapiro E. M., Maric D., Conroy R., and Koretsky A. P. (2009) In vivo labeling of adult neural progenitors for MRI with micron sized particles of iron oxide: quantification of labeled cell phenotype. *NeuroImage* **44**, 671–8.
33. Yang J., Liu J., Niu G., et al. (2009) In vivo MRI of endogenous stem/progenitor cell migration from subventricular zone in normal and injured developing brains. *NeuroImage* **48**, 319–28.
34. Berry C. J., Thedens D. R., Light-McGroary K., et al. (2009) Effects of deep sedation or general anesthesia on cardiac function in mice undergoing cardiovascular magnetic resonance. *J Cardiovas Magn Reson* **11**, 16.
35. Qiu H. H., Cofer G. P., Hedlund L. W., and Johnson G. A. (1997) Automated feedback control of body temperature for small animal studies with MR microscopy. *IEEE Trans Biomed Eng* **44**, 1107–13.
36. Dazai J., Bock N. A., Nieman B. J., Davidson L. M., Henkelman R. M., and Chen X. J. (2004) Multiple mouse biological loading and monitoring system for MRI. *Magn Reson Med* **52**, 709–15.
37. Boretius S., Michaelis T., Tammer R., Ashery-Padan R., Frahm J., and Stoykova A. (2009) In vivo MRI of altered brain anatomy and fiber connectivity in adult pax6 deficient mice. *Cerebral Cortex* **19**, 2838–47.
38. Cheung M. M., Hui E. S., Chan K. C., Helpern J. A., Qi L., and Wu E. X. (2009) Does diffusion kurtosis imaging lead to better neural tissue characterization? A rodent brain maturation study. *NeuroImage* **45**, 386–92.
39. Jensen J. H., Helpern J. A., Ramani A., Lu H., and Kaczynski K. (2005) Diffusional kurtosis imaging: the quantification of non-gaussian water diffusion by means of magnetic resonance imaging. *Magn Reson Med* **53**, 1432–40.

40. So P.-W., Yu W.-S., Kuo Y.-T., et al. (2007) Impact of resistant starch on body fat patterning and central appetite regulation. *PloS One* **2**, e1309.
41. Hegedus B., Hughes F. W., Garbow J. R., et al. (2009) Optic nerve dysfunction in a mouse model of neurofibromatosis-1 optic glioma. *J Neuropath Exp Neurol* **68**, 542–51.
42. Kim J. H., Budde M. D., Liang H.-F., et al. (2006) Detecting axon damage in spinal cord from a mouse model of multiple sclerosis. *Neurobiol Dis* **21**, 626–32.
43. Kalber T. L., Waterton J. C., Griffiths J. R., Ryan A. J., and Robinson S. P. (2008) Longitudinal in vivo susceptibility contrast MRI measurements of LS174T colorectal liver metastasis in nude mice. *J Magn Reson Imaging* **28**, 1451–8.
44. Sakata N., Hayes P., Tan A., et al. (2009) MRI assessment of ischemic liver after intraportal islet transplantation. *Transplantation* **87**, 825–30.
45. Sadick M., Schock D., Kraenzlin B., Gretz N., Schoenberg S. O., and Michaely H. J. (2009) Morphologic and dynamic renal imaging with assessment of glomerular filtration rate in a pcy-mouse model using a clinical 3.0 Tesla scanner. *Invest Radiol* **44**, 469–75.
46. Jennbacken K., Gustavsson H., Tesan T., et al. (2009) The prostatic environment suppresses growth of androgen-independent prostate cancer xenografts: an effect influenced by testosterone. *Prostate* **69**, 1164–75.
47. Olive K. P., Jacobetz M. A., Davidson C. J., et al. (2009) Inhibition of Hedgehog signaling enhances delivery of chemotherapy in a mouse model of pancreatic cancer. *Science (New York, N.Y.)* **324**, 1457–61.
48. Berr S. S., Roy R. J., French B. A., et al. (2005) Black blood gradient echo cine magnetic resonance imaging of the mouse heart. *Magn Reson Med* **53**, 1074–9.
49. Cassidy P. J., Schneider J. E., Grieve S. M., Lygate C., Neubauer S., and Clarke K. (2004) Assessment of motion gating strategies for mouse magnetic resonance at high magnetic fields. *J Magn Reson Imaging* **19**, 229–37.
50. Wiesmann F., Frydrychowicz A., Rautenberg J., et al. (2002) Analysis of right ventricular function in healthy mice and a murine model of heart failure by in vivo MRI. *Am J Physiol Heart Circ Phys* **283**, H1065–71.
51. Heijman E., Graaf W. D., Niessen P., and Nauerth A. (2007) Comparison between prospective and retrospective triggering for mouse cardiac MRI. *NMR Biomed* **20**, 439–47.
52. Hiba B., Richard N., Janier M., and Croisille P. (2006) Cardiac and respiratory double self-gated cine MRI in the mouse at 7 T. *Magn Reson Med* **55**, 506–13.
53. Bishop J., Feintuch A., Bock N. A., et al. (2006) Retrospective gating for mouse cardiac MRI. *Magn Reson Med* **55**, 472–7.
54. Bucholz E., Ghaghada K., Qi Y., Mukundan S., and Johnson G. A. (2008) Four-dimensional MR microscopy of the mouse heart using radial acquisition and liposomal gadolinium contrast agent. *Magn Reson Med* **60**, 111–8.
55. Feintuch A., Zhu Y., Bishop J., Davidson L., and Dazai J. (2007) 4D cardiac MRI in the mouse. *NMR Biomed* **5**, 360–5.
56. Ross A. J., Yang Z., Berr S. S., et al. (2002) Serial MRI evaluation of cardiac structure and function in mice after reperfused myocardial infarction. *Magn Reson Med* **47**, 1158–68.
57. Franco F., Thomas G. D., Giroir B., et al. (1999) Magnetic resonance imaging and invasive evaluation of development of heart failure in transgenic mice with myocardial expression of tumor necrosis factor-alpha. *Circulation* **99**, 448–54.
58. Nahrendorf M., Spindler M., Hu K., et al. (2005) Creatine kinase knockout mice show left ventricular hypertrophy and dilatation, but unaltered remodeling post-myocardial infarction. *Cardiovas Res* **65**, 419–27.
59. Schneider J. E., Stork L.-A., Bell J. T., et al. (2008) Cardiac structure and function during ageing in energetically compromised guanidinoacetate *N*-methyltransferase (GAMT)-knockout mice—a one year longitudinal MRI study. *J Cardiovas Magn Reson* **10**, 9.
60. Ten Hove M., Lygate C. A., Fischer A., et al. (2005) Reduced inotropic reserve and increased susceptibility to cardiac ischemia/reperfusion injury in phosphocreatine-deficient guanidinoacetate-*N*-methyltransferase-knockout mice. *Circulation* **111**, 2477–85.
61. Olsson L. E., Smailagic A., Onnervik P.-O., and Hockings P. D. (2009) (1)H and hyperpolarized (3)He MR imaging of mouse with LPS-induced inflammation. *J Magn Reson Imaging* **29**, 977–81.
62. Thomas A. C., Potts E. N., Chen B. T., Slipetz D. M., Foster W. M., and Driehuys B. (2009) A robust protocol for regional evaluation of methacholine challenge in

mouse models of allergic asthma using hyperpolarized ^{3}He MRI. *NMR Biomed* **22**, 502–15.
63. Wakayama T., Narazaki M., Kimura A., and Fujiwara H. (2008) Hyperpolarized ^{129}Xe phase-selective imaging of mouse lung at 9.4T using a continuous-flow hyperpolarizing system. *Magn Reson Med Sci* **7**, 65–72.
64. Sheth V. R., van Heeckeren R. C., Wilson A. G., and AM (2008) Monitoring infection and inflammation in murine models of cystic fibrosis with magnetic resonance imaging. *J Magn Reson Imaging* **28**, 527–32.
65. Watt K. N., Bishop J., Nieman B. J., Henkelman R. M., and Chen X. J. (2008) Oxygen-enhanced MR imaging of mice lungs. *Magn Reson Med* **59**, 1412–21.
66. Chen B. T., Yordanov A. T., and Johnson G. A. (2005) Ventilation-synchronous magnetic resonance microscopy of pulmonary structure and ventilation in mice. *Magn Reson Med* **53**, 69–75.
67. Carreno B. M., Garbow J. R., Kolar G. R., et al. (2009) Immunodeficient mouse strains display marked variability in growth of human melanoma lung metastases. *Clin Cancer Res* **15**, 3277–86.
68. Engelman J. A., Chen L., Tan X., Crosby K., and Guimaraes A.R. (2008) Effective use of PI3K and MEK inhibitors to treat mutant Kras G12D and PIK3CA H1047R murine lung cancers. *Nature Med* **14**, 1351–6.
69. Li L. Z., Zhou R., Xu H. N., et al. (2009) Quantitative magnetic resonance and optical imaging biomarkers of melanoma metastatic potential. *PNAS* **106**, 6608–13.
70. Blé F. -X., Cannet C., Zurbruegg S., et al. (2008) Allergen-induced lung inflammation in actively sensitized mice assessed with MR imaging. *Radiology* **248**, 834–43.
71. Alsaid H., Sabbah M., Bendahmane Z., et al. (2007) High-resolution contrast-enhanced MRI of atherosclerosis with digital cardiac and respiratory gating in mice. *Magn Reson Med* **58**, 1157–63.
72. Chaabane L., Pellet N., Bourdillon M. C., Desbleds-Mansard C., Sulaiman A., Hadour G., Thivolet-Béjui F., Roy P., Briguet A., Douek P., and Canet-Soulas E. (2004) Contrast enhancement in atherosclerosis development in a mouse model: in vivo results at 2 Tesla. *Magma* **17**, 188–95.
73. Cha S., Johnson G., Wadghiri Y. Z., et al. (2003) Dynamic, contrast-enhanced perfusion MRI in mouse gliomas: correlation with histopathology. *Magn Reson Med* **49**, 848–55.
74. Checkley D., Tessier J. J. L., Wedge S. R., et al. (2003) Dynamic contrast-enhanced MRI of vascular changes induced by the VEGF-signalling inhibitor ZD4190 in human tumour xenografts. *Magn Reson Imaging* **21**, 475–82.
75. Kiselev V. G., Strecker R., Ziyeh S., Speck O., and Hennig J. (2005) Vessel size imaging in humans. *Magn Reson Med* **53**, 553–63.
76. Neeman M. and Dafni H. (2003) Structural, functional, and molecular MR imaging of the microvasculature. *Ann Rev Biomed Eng* **5**, 29–56.
77. Zwick S., Strecker R., Kiselev V., et al. (2009) Assessment of vascular remodeling under antiangiogenic therapy using DCE-MRI and vessel size imaging. *J Magn Reson Imaging* **29**, 1125–33.
78. Yu X., Wadghiri Y. Z., Sanes D. H., and Turnbull D. H. (2005) In vivo auditory brain mapping in mice with Mn-enhanced MRI. *Nature Neurosci* **8**, 961–8.
79. Yu X., Sanes D. H., Aristizabal O., Wadghiri Y. Z., and Turnbull D. H. (2007) Large-scale reorganization of the tonotopic map in mouse auditory midbrain revealed by MRI. *PNAS* **104**, 12193–8.
80. Pautler R. G. and Koretsky A. P. (2002) Tracing odor-induced activation in the olfactory bulbs of mice using manganese-enhanced magnetic resonance imaging. *NeuroImage* **16**, 441–8.
81. Watanabe T., Radulovic J., Spiess J., et al. (2004) In vivo 3D MRI staining of the mouse hippocampal system using intracerebral injection of $MnCl_2$. *NeuroImage* **22**, 860–7.
82. Smith K. D. B., Kallhoff V., Zheng H., and Pautler R. G. (2007) In vivo axonal transport rates decrease in a mouse model of Alzheimer's disease. *NeuroImage* **35**, 1401–8.
83. Cohen B., Dafni H., Meir G., Harmelin A., and Neeman M. (2005) Ferritin as an endogenous MRI reporter for noninvasive imaging of gene expression in C6 glioma tumors. *Neoplasia* **7**, 109–17.
84. Deans A. E., Wadghiri Y. Z., Bernas L. M., Yu X., Rutt B. K., and Turnbull D. H. (2006) Cellular MRI contrast via coexpression of transferrin receptor and ferritin. *Magn Reson Med* **56**, 51–9.
85. Genove G., DeMarco U., Xu H., Goins W. F., and Ahrens E. T. (2005) A new transgene reporter for in vivo magnetic resonance imaging. *Nature Med* **11**, 450–4.
86. Gilad A. A., McMahon M. T., Walczak P., et al. (2007) Artificial reporter gene

providing MRI contrast based on proton exchange. *Nature Biotechnol* **25**, 217–9.
87. Gilad A. A., Winnard P. T., Van Zijl P. C. M., and Bulte J. W. M. (2007) Developing MR reporter genes: promises and pitfalls. *NMR Biomed* **20**, 275–90.
88. Weissleder R., Moore A., Mahmood U., et al. (2000) In vivo magnetic resonance imaging of transgene expression. *Nature Med* **6**, 351–5.
89. Zurkiya O., Chan A. W. S., and Hu X. (2008) MagA is sufficient for producing magnetic nanoparticles in mammalian cells, making it an MRI reporter. *Magn Reson Med* **59**, 1225–31.
90. Zhao M., Beauregard D. A., Loizou L., Davletov B., and Brindle K. M. (2001) Non-invasive detection of apoptosis using magnetic resonance imaging and a targeted contrast agent. *Nature Med* **7**, 1241–4.
91. Burtea C., Laurent S., Murariu O., et al. (2008) Molecular imaging of alpha v beta3 integrin expression in atherosclerotic plaques with a mimetic of RGD peptide grafted to Gd-DTPA. *Cardiovas Res* **78**, 148–57.
92. Winter P. M., Caruthers S. D., Yu X., et al. (2003) Improved molecular imaging contrast agent for detection of human thrombus. *Magn Reson Med* **50**, 411–6.
93. Larbanoix L., Burtea C., Laurent S., et al. (2008) Potential amyloid plaque-specific peptides for the diagnosis of Alzheimer's disease. *Neurobiol Aging* **31**, 1679–89.
94. Burtea C., Laurent S., Port M., et al. (2009) Magnetic resonance molecular imaging of vascular cell adhesion molecule-1 expression in inflammatory lesions using a peptide-vectorized paramagnetic imaging probe. *J Med Chem* **52**, 4725–42.
95. Anderson S. A., Shukaliak-Quandt J., Jordan E. K., et al. (2004) Magnetic resonance imaging of labeled T-cells in a mouse model of multiple sclerosis. *Ann Neurol* **55**, 654–9.
96. Bulte J. W. M. and Kraitchman D. L. (2004) Monitoring cell therapy using iron oxide MR contrast agents. *Curr Pharm Biotechnol* **5**, 567–84.
97. Heyn C., Ronald J. A., Mackenzie L. T., et al. (2006) In vivo magnetic resonance imaging of single cells in mouse brain with optical validation. *Magn Reson Med* **55**, 23–9.
98. Magnitsky S., Watson D. J., Walton R. M., et al. (2005) In vivo and ex vivo MRI detection of localized and disseminated neural stem cell grafts in the mouse brain. *NeuroImage* **26**, 744–54.
99. Shapiro E. M., Skrtic S., Sharer K., Hill J. M., Dunbar C. E., and Koretsky A. P. (2004) MRI detection of single particles for cellular imaging. *PNAS* **101**, 10901–6.
100. Johnson G. A., Cofer G. P., Gewalt S. L., and Hedlund L. W. (2002) Morphologic phenotyping with MR microscopy: the visible mouse. *Radiology* **222**, 789–93.
101. Zhou Y. Q., Davidson L., Henkelman R. M., et al. (2004) Ultrasound-guided left-ventricular catheterization: a novel method of whole mouse perfusion for microimaging. *Lab Invest* **84**, 385–9.
102. Dorr A., Lerch J. P., Spring S., Kabani N., and Henkelman R. (2008) High resolution three-dimensional brain atlas using an average magnetic resonance image of 40 adult C57Bl/6 J mice. *NeuroImage* **42**, 60–9.
103. Kovacević N., Henderson J. T., Chan E., et al. (2005) A three-dimensional MRI atlas of the mouse brain with estimates of the average and variability. *Cerebral Cortex* **15**, 639–45.
104. Lerch J. P., Carroll J., Spring S., et al. (2008) Automated deformation analysis in the YAC128 Huntington disease mouse model. *NeuroImage* **39**, 32–9.
105. Lerch J. P., Yiu A. P., Bohbot V. D., Henkelman R. M., Josseyln S. A., and Sled J. G. (2008) MRI can detect brain shape changes in mice caused by five days of learning. *International Society of Magnetic Resonance in Medicine 16th Scientific Meeting* 479.
106. Maheswaran S., Barjat H., Rueckert D., et al. (2009) Longitudinal regional brain volume changes quantified in normal aging and Alzheimer's APP x PS1 mice using MRI. *Brain Res* **1270**, 19–32.
107. Persson A.-S., Westman E., Wang F.-H., Khan F. H., Spenger C., and Lavebratt C. (2007) Kv1.1 null mice have enlarged hippocampus and ventral cortex. *BMC Neurosci* **8**, 10.
108. Thompson P. M., MacDonald D., Mega M. S., Holmes C. J., Evans A. C., and Toga A. W. (1997) Detection and mapping of abnormal brain structure with a probabilistic atlas of cortical surfaces. *J Comp Ass Tom* **21**, 567–81.
109. Chung M. K., Worsley K. J., Paus T., et al. (2001) A unified statistical approach to deformation-based morphometry. *NeuroImage* **14**, 595–606.
110. Lepore N., Brun C. A., Chiang M.-C., et al. (2006) Multivariate statistics of the Jacobian matrices in tensor based morphometry and their application to HIV/AIDS. *Med Image*

Comput Comput Assist Interv Int Conf **9**, 191–8.
111. Kim H., Besson P., Colliot O., Bernasconi A., and Bernasconi N. (2008) Surface-based vector analysis using heat equation interpolation: a new approach to quantify local hippocampal volume changes. *Med Image Comput Comput Assist Interv Int Conf* **11**, 1008–15.
112. Cao J. and Worsley K. J. (1999) The detection of local shape changes via the geometry of Hotelling's T-2 fields. *Ann Stat* **27**, 925–42.
113. Nieman B. J., Flenniken A. M., Adamson S. L., Henkelman R. M., and Sled J. G. (2006) Anatomical phenotyping in the brain and skull of a mutant mouse by magnetic resonance imaging and computed tomography. *Physiol Genomics* **24**, 154–62.
114. Clapcote S. J., Lipina T. V., Millar J. K., et al. (2007) Behavioral phenotypes of Disc1 missense mutations in mice. *Neuron* **54**, 387–402.
115. Nichols T. E. and Holmes A. P. (2002) Nonparametric permutation tests for functional neuroimaging: a primer with examples. *Hum Brain Mapp* **15**, 1–25.
116. Lerch J. P., Carroll J. B., Dorr A., et al. (2008) Cortical thickness measured from MRI in the YAC128 mouse model of Huntington's disease. *NeuroImage* **41**, 243–51.
117. Meadowcroft M. D., Connor J. R., Smith M. B., and Yang Q. X. (2009) MRI and histological analysis of beta-amyloid plaques in both human Alzheimer's disease and APP/PS1 transgenic mice. *J Magn Reson Imaging* **29**, 997–1007.
118. Kale S. C., Lerch J. P., Henkelman R. M., and Chen X. J. (2008) Optimization of the SNR-resolution tradeoff for registration of magnetic resonance images. *Hum Brain Mapp* **29**, 1147–58.
119. Nieman B. J., Bock N. A., Bishop J., Sled J. G., Chen X. J., and Henkelman R. M. (2005) Fast spin-echo for multiple mouse magnetic resonance phenotyping. *Magn Reson Med* **54**, 532–7.
120. Chaabane L., Pellet N., Bourdillon M. C., et al. (2004) Contrast enhancement in atherosclerosis development in a mouse model: in vivo results at 2 Tesla. *Magma* **17**, 188–95.
121. Lau J. C., Lerch J. P., Sled J. G., Henkelman R. M., Evans A. C., and Bedell B. J. (2008) Longitudinal neuroanatomical changes determined by deformation-based morphometry in a mouse model of Alzheimer's disease. *NeuroImage* **42**, 19–27.
122. Nieman B. J., Bock N. A., Bishop J., et al. (2005) Magnetic resonance imaging for detection and analysis of mouse phenotypes. *NMR Biomed* **18**, 447–68.